

AD-A230 556

NONLINEAR INTERFEROMETRY:  
OPTICAL IMAGE ADDITION/SUBTRACTION  
AND NOVELTY FILTERS

THESIS

Gordon Thomas Hengst  
Captain, USAF

AFIT/GEO/ENP/90D-2

RECEIVED

DEPARTMENT OF THE AIR FORCE  
AIR UNIVERSITY

AIR FORCE INSTITUTE OF TECHNOLOGY

Wright-Patterson Air Force Base, Ohio

91 113 102

AFIT/GEO/ENP/90D-2



NONLINEAR INTERFEROMETRY:  
OPTICAL IMAGE ADDITION/SUBTRACTION  
AND NOVELTY FILTERS

THESIS

Gordon Thomas Hengst  
Captain, USAF

AFIT/GEO/ENP/90D-2

*APPROVED FOR PUBLIC RELEASE; DISTRIBUTION UNLIMITED.*

AFIT/GEO/ENP/90D-2

NONLINEAR INTERFEROMETRY:  
OPTICAL IMAGE ADDITION/SUBTRACTION  
AND NOVELTY FILTERS

THESIS

Presented to the Faculty of the School of Engineering  
of the Air Force Institute of Technology  
Air University  
In Partial Fulfillment of the  
Requirements for the Degree of  
Master of Science in Electrical Engineering

Gordon Thomas Hengst, B.S.  
Captain, USAF

December, 1990

Accession No.	
NTIS GPO/AF	
DNC TAL	
Unpublished	
JAN 1991	
By	
Distribution	
Availability	
Dist	
A-1	

APPROVED FOR PUBLIC RELEASE; DISTRIBUTION UNLIMITED.

## *Table of Contents*

	Page
Table of Contents . . . . .	ii
List of Figures . . . . .	iv
List of Tables . . . . .	vi
Abstract . . . . .	vii
I. Introduction . . . . .	1
II. Previous Experimental Work on Novelty Filtering and Optical Image Subtraction/Addition . . . . .	3
2.1 Michelson Interferometer Novelty Filter . . . . .	3
2.2 Beam Fanning Novelty Filter . . . . .	6
2.3 Two-Beam Coupling Novelty Filter . . . . .	8
2.4 Optical Image Addition/Subtraction . . . . .	9
III. Materials and Equipment . . . . .	12
IV. System Parameters Which Characterize Novelty Filters and the Experi- mental Set-up . . . . .	13
4.1 Novelty Filter System Parameters . . . . .	13
4.1.1 Spatial Resolution. . . . .	13
4.1.2 Contrast Ratio. . . . .	14
4.1.3 Onset Time. . . . .	14
4.1.4 Velocity Response of the Crystal. . . . .	15
4.2 Beam Fanning Experimental Set-up . . . . .	16

	Page
4.2.1 Spatial Resolution. . . . .	16
4.2.2 Contrast Ratio. . . . .	16
4.2.3 Onset Time . . . . .	16
4.2.4 Velocity Response. . . . .	17
V. Beam Fanning Novelty Filter Results and Discussion . . . . .	18
5.1 Spatial Resolution . . . . .	18
5.2 Contrast Ratio . . . . .	20
5.3 Onset Time . . . . .	22
5.4 Velocity Response . . . . .	25
VI. Switchable Optical Adder/Subtractor: Theoretical Analysis and Experimental Set-up . . . . .	28
VII. Switchable Adder/Subtractor Results and Discussion . . . . .	31
VIII. Conclusions & Recommendations . . . . .	36
8.1 Beam Fanning Novelty Filter . . . . .	36
8.2 Switchable Adder/Subtractor . . . . .	38
Appendix A. General References . . . . .	40
Appendix B. Computer Generated Holograms . . . . .	42
B.1 Program . . . . .	42
B.2 Photoreduction of Holograms . . . . .	44
B.3 Tips On Hologram Usage . . . . .	46
Appendix C. Experimental Procedure for Determining Onset Time . . . . .	48
Bibliography . . . . .	50
Vita . . . . .	52

## *List of Figures*

Figure	Page
1. Michelson interferometer novelty filters. (a) Phase modulated input signal, (b) Polarization modulated input signal. (2:641) . . . . .	4
2. A Michelson interferometer using two self-pumped crystals for phase-conjugation. (8:283) . . . . .	6
3. Beam fanning novelty filter. . . . .	7
4. Two-beam coupling novelty filter. . . . .	9
5. Optical image adder/subtractor with a Michelson interferometer. Port A contains image subtraction and addition is seen output at Port B. (4:306)	10
6. An optical image adder/subtractor using polarization. (15:425) . . .	11
7. Experimental set-up to examine the spatial resolution of a beam fanning novelty filter. . . . .	13
8. Scenario relating an object's transverse speed in the real world to the input plane of reference of a novelty filter. In this case, an object moving at 100 km/hr translates to 0.52 mm/sec in the input plane. .	15
9. Experimental set-up to examine the spatial resolution limit of the beam fanning novelty filter. . . . .	17
10. Fourier spectrums of an AF resolution chart using a beam fanning novelty filter. (a) Unfiltered spectrum, (b) Spectrum after being filtered by Crystal 115- F, (c) Spectrum filtered by Crystal 119-D, (d) Spectrum filtered by Crystal 127-K. . . . .	19
11. Experimental results for the Contrast Ratio, C. The dotted line represents a linear interpolation of the curves. . . . .	21
12. Experimental results for the Onset Time experiments. . . . .	23
13. Unexplained onset behavior of crystal 127-K at powers greater than 26 mW. . . . .	23
14. A filtered output of a "T" as it moved to the right followed closely by its ghost. . . . .	25

Figure	Page
15. Minimum velocities for each of the three crystals. Maximum velocities were unattainable due to the limitation of the stepper motor. . . . .	26
16. Schematic diagram of the switchable optical image adder/subtractor designed in the thesis. . . . .	28
17. Intensity detected at the output port of the switchable adder/subtractor. (a) Lower leg full intensity, (b) Image subtraction, (c) Upper leg full intensity, (d) Image addition. . . . .	32
18. Optical image addition and subtraction. (a) A circle and square are subtracted when Switch 1 is open, (b) cross-sectional profile showing the subtraction, (c) image addition with Switch 1 closed, (d) cross-sectional profile showing addition. . . . .	35
19. An alternate configuration for the switchable optical adder/subtractor.	39
20. A sinusoidal computer generated hologram showing 4 cycles . . . . .	44
21. Dekacon photoreduction system. (14:43) . . . . .	45
22. Intensity profile of a 4 cycle computer generated hologram showing the sinusoidal profile. The gaussian profile of the laser beam incident on the hologram is shown by the dotted line. . . . .	47
23. Experimental set-up to determine the onset time for each crystal. . .	49
24. Sample filter trace to determine the crystal's onset time, $\tau_{filter}$ . . . .	49

### *List of Tables*

Table	Page
1. BaTiO <sub>3</sub> crystals used in the thesis. . . . .	12
2. Highest spatial frequencies obtained from an unfiltered and filtered AF resolution chart using a beam fanning novelty filter. . . . .	18
3. Qualitative summary of the beam fanning novelty filter portion of the thesis. . . . .	36
4. Resolutions of computer generated holograms obtained using a 50% reduced transparency and 60X photoreduction . . . . .	46



*Abstract*

This thesis investigated the performance characteristics of a beam fanning novelty filter and designed a switchable optical image adder/subtractor. The filter spatial resolution, contrast ratio, onset time, and velocity response were measured for both z-cut and 45°-cut BaTiO<sub>3</sub> crystals in the beam fanning configuration. Experimental results show that the special 45°-cut crystal produces the best overall beam fanning novelty filter. In addition, switchable optical image subtraction and addition were demonstrated for the first time using a modified Michelson interferometer configured with a phase-conjugating mirror and an adjustable length leg. The system demonstrated addition and subtraction with one-dimensional and two-dimensional images. The adder/subtractor can be switched from coherent subtraction to incoherent addition by biasing a set of e-o crystals which switches the beam in one of the legs of the interferometer into an extra length. The extra length is greater than the coherence length of the laser so that incoherent addition results. The thesis concludes with a brief discussion of industrial and military system applications of the novelty filter and adder/subtractor.

# NONLINEAR INTERFEROMETRY: OPTICAL IMAGE ADDITION/SUBTRACTION AND NOVELTY FILTERS

## *I. Introduction*

Nonlinear interferometry has been used in a variety of applications ranging from optical amplifiers to image processing. Two of these techniques, beam fanning novelty filtering and optical image addition/subtraction, are investigated in this thesis research. Both of these techniques are vital to advanced weapon systems.

Automated weapon systems rely heavily on target classification and identification which, in turn, requires the ability to extract moving objects from a scene and to add and subtract two images during processing. By segmenting an image into moving and stationary objects, a target classifier can concentrate more processing time on the smaller image space that moving objects occupy within an entire scene. This allows the moving object to be identified more accurately and efficiently. By adding and subtracting images optically, processing speeds can be increased, while processor weight and power requirements are reduced. Currently, object segmentation and image processing is done using video image subtraction/addition. A video frame is subtracted or added, pixel-by-pixel, from the previous frame to yield new or changing information.

Image processing can be done more efficiently optically because of the parallel nature of light. Both optical novelty filtering, i.e. the filtering of new or changing information, and image addition/subtraction have been demonstrated using phase conjugation, two-wave mixing and beam fanning techniques. However, the important issues concerning Air Force weapon systems have not been addressed in the

literature, to date. Therefore, of the three types of novelty filtering, 1) Michelson interferometer, 2) two-wave mixing and 3) beam fanning, the beam fanning technique was chosen for investigation in this thesis since a specially cut nonlinear crystal with excellent fanning properties was available. The adder/subtractor will utilize a modified Michelson interferometer that has an adjustable length leg for coherent image subtraction and incoherent image addition.

The objective of this thesis is to characterize the beam fanning method of creating an optical novelty filter and to characterize the switchable adder/subtractor. The filter will be characterized by its spatial resolution, contrast ratio, onset time, and velocity response, while the adder/subtractor will be characterized by its ability to properly add and subtract both one-dimensional and two-dimensional images. From these results, it can be determined how the filter system is best suited for moving target recognition preprocessing, signal processing, and other military applications and also the usefulness of the adder/subtractor in various military systems.

The thesis begins in Chapter II with an overview of optical novelty filtering and image addition and subtraction. The various BaTiO<sub>3</sub> crystals and other materials and equipment are discussed in Chapter III. Chapter IV describes the system parameters to be measured and the experimental set-up for the beam fanning novelty filter configuration investigated in the thesis. Experimental results and discussion of the results are presented in Chapter V. The theory and experimental setup for the switchable optical adder/subtractor and experimental results and conclusions are discussed in Chapters VI and VII, respectively. The final chapter gives an evaluation as to how the filter system and the optical adder/subtractor investigated in the thesis can be used in military applications and other conclusions that can be drawn from the experimental data. Additional references not specifically cited in the thesis are listed in Appendix A. These sources provided additional background information necessary to fully understand the concepts discussed in this thesis.

## *II. Previous Experimental Work on Novelty Filtering and Optical Image Subtraction/Addition*

Current research in optical novelty filters can be categorized into three different techniques. These techniques include Michelson interferometers, beam fanning, and two-wave mixing using either  $\text{BaTiO}_3$ , BSO or other nonlinear photorefractive crystals.

### *2.1 Michelson Interferometer Novelty Filter*

Traditionally, a Michelson interferometer is thought of as having two conventional flat mirrors to retro-reflect the interferometer's legs back upon themselves to allow coherent interference. The legs of the traditional Michelson interferometer must be the exact same length with strict tolerance. In addition, the optics in the interferometer, including flats and mirrors, must be of excellent quality since any aberration caused by them will be doubled when the beams in the legs pass through them twice.

In contrast, a Michelson interferometer configured with a phase-conjugating mirror (PCM), instead of two flat mirrors, compensates many of the restrictions imposed on a traditional interferometer. With a PCM, the wave front retraces its path instead of being retro-reflected and therefore un-aberrate themselves, recreating the original phase front at the beam splitter. Since the wavefront at the beamsplitter is recreated, the length of the legs need not be equal, as long as the difference between the two legs is within the coherence length of the laser. Compensating for the restrictions of the traditional Michelson interferometer allows the PCM interferometer to be an excellent and easily constructed novelty filter.

The Michelson interferometer using phase-conjugation is the most widely documented novelty filter. When the legs of the interferometer are phase-conjugated, the

phase at the entrance to the interferometer can be easily recreated causing destructive interference necessary for the filter. Phase-conjugation can be achieved either by self-pumping (2:640-643) or by externally-pumping (3:652) a nonlinear crystal, with self-pumping being the most commonly used technique. Jack Feinberg first demonstrated, in 1982, the simple technique of creating a self-pumped continuous-wave phase-conjugator using internal reflection within a  $\text{BaTiO}_3$  crystal (9:486). The ease of this technique of creating a phase-conjugate beam makes this ideal for an interferometer, since the relative phase matching of the two interferometer legs is less sensitive to vibrations, air disturbances, and optical component distortions (10:509).

With a Michelson filter, the input signal or image to be filtered is modulated using either a phase or polarization modulator as shown in Figure 1. Amplitude

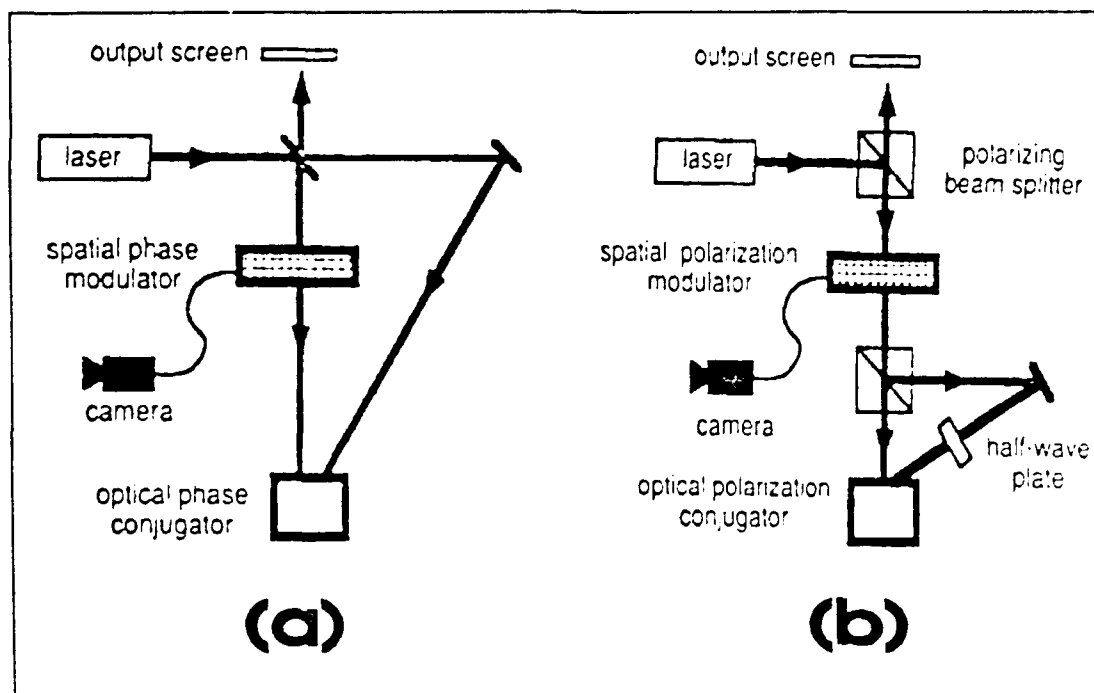


Figure 1. Michelson interferometer novelty filters. (a) Phase modulated input signal. (b) Polarization modulated input signal. (2:641)

modulation is not applicable in this configuration since it would produce a contrast reversed image in the steady state condition rather than blocking stagnant objects. A more complete discussion of the coherent image subtraction process is included

in Chapter VI. For the phase modulated signal shown in Figure 1a, the plane wave from the laser is split into two legs entering into the interferometer. In one leg the beam is unaltered, while in the other leg the beam passes through a phase modulator, such as a Pockels cell or a LCTV with its analyzer removed. Both beams are phase-conjugated, via self-pumping in the same crystal, and therefore, propagate back toward the beamsplitter. In steady state conditions, the information on the phase modulated signal is exactly canceled since the conjugated beam will have achieved its original phase front at the beamsplitter. The two beams recombine and exactly cancel each other so no light emerges from the output port. However, if the image on the modulator should change in a time shorter than the onset time of the crystal, the beam retracing back through the phase modulator will not reconstruct its original phase front. Therefore, when the two beams recombine back at the beamsplitter, there will be an output signal at the portion of the image where the wavefront has changed, since the wavefronts no longer exactly cancel each other at these points (2:640). The end result at these specific points is incoherent image addition as described in Chapter VI with one leg having a constant amplitude and the other leg modulated by the image. The rest of the image (i.e., the stagnant portions) remain in phase with the other leg and therefore are coherently subtracted out of the image.

The polarization modulated signal, shown in Figure 1b, is similar to the phase modulated process described above. In this case, the laser beam is deflected using a polarizing beamsplitter (which also serves as the output port of the filter), modulated and then split into the Michelson interferometer using a second polarizing beamsplitter. The half-wave plate in the interferometer is used to convert the vertically polarized arm to horizontal polarization so that self-pumping will occur in the crystal. In the steady state case, the input signal, after being modulated and conjugated, returns to the first polarizing beamsplitter with its initial polarization, and therefore, will be reflected back toward the laser. However, if portions of the

signal in the modulator should change, the polarization of the conjugated signal will be altered and those portions will be passed by the first beamsplitter as an output to the filter.(1:124)

Both Michelson interferometer filter techniques described above use a single crystal for phase-conjugating both legs of the interferometer. An alternate technique for phase-conjugating each leg has been demonstrated by Ewbank *et al* and is shown in Figure 2. Two self-pumped crystals, one for each leg, are used. A spontaneously generated self-oscillation between the crystals, as shown in the figure, locks the relative phase between the two legs. Since the relative phase is locked, total destructive interference can be achieved at the beamsplitter. (8:282-283)

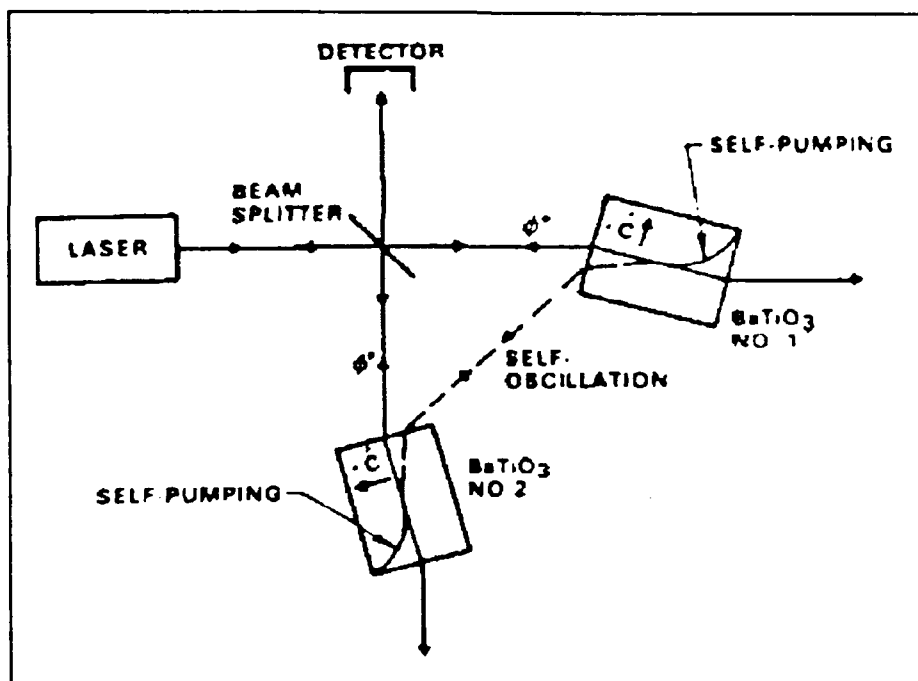


Figure 2. A Michelson interferometer using two self-pumped crystals for phase-conjugation. (8:283)

## 2.2 Beam Fanning Novelty Filter

Although the majority of the literature concerns the Michelson designs, there is a second type of novelty filter that was demonstrated by Joseph E. Ford *et al*

using photorefractive fanout (11:856-858) as shown in Figure 3. This technique uses: "... a time integrating interferometer that effectively subtracts an exponential

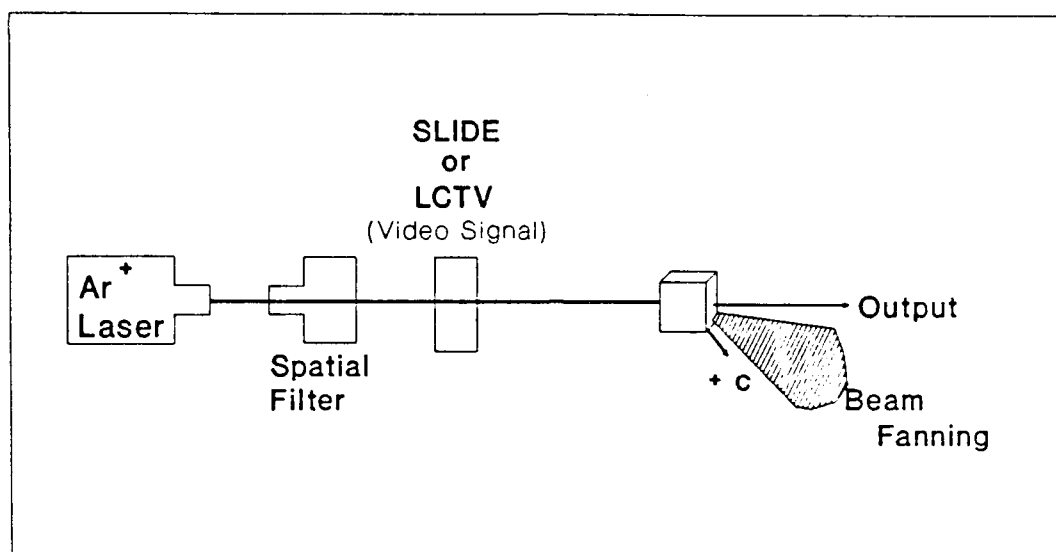


Figure 3. Beam fanning novelty filter.

weighted history of a two-dimensional input field from its current value" as described by the equation (11:856):

$$I(t) = I(o) \left[ \frac{1 + m_o}{1 + m_o \exp(\Gamma_{eff}(t)L)} \right] \quad (1)$$

$$\Gamma_{eff} = \Gamma_o [1 - \exp(-t/\tau)] \quad (2)$$

where

- $I(t)$  = Filter output intensity
- $I(o)$  = Incident intensity
- $m_o$  = Initial scattered fraction of the input beam intensity
- $\Gamma_{eff}$  = Effective gain coefficient of the crystal
- $\Gamma_o$  = Photorefractive gain coefficient
- $\tau$  = Photorefractive response time ( $\tau_{filter}$ )
- $L$  = Interaction length



The longer in time the signal beam remains constant, the stronger the exponential subtraction becomes. Therefore, this device can act as a novelty filter, since the new parts of the image are passed and old information is subtracted out, thus fulfilling the definition of a novelty filter. Also, the filter is responsive to an amplitude modulated signal in addition to phase and polarization modulated signals. Theoretically, any change in the signal that would disturb the index grating should cause an output to the filter. (11:856)

This device differs from the Michelson interferometer configurations, in that it relies on signal depletion rather than destructive interference. The fanning process in the crystal is a two step process. Ford *et al* describes the first step as "Scattering of coherent light from imperfections and impurities in the crystal" which is then followed by amplification of the scattered photons via two-beam coupling. The noise, i.e. beam fanning, grows at the expense of the signal beam, which eventually is depleted. (11:856)

In order to achieve complete signal depletion, Equation (1) requires a crystal with the maximum gain possible. Maximum gain in the BaTiO<sub>3</sub> crystal occurs when the input signal propagates through the crystal such that the grating wave vectors are oriented at 45° to the optic axis. In their experiments, Ford *et al* used a specially cut crystal whose c-axis was at 45° to the crystal face. This maximizes the gain for near-normal signal incidence and reduces reflection and refraction losses. BaTiO<sub>3</sub> crystals are normally cut with the c-axis parallel to one of the crystal's edges. This is the type which is commonly used in the Michelson configurations described above.

### 2.3 Two-Beam Coupling Novelty Filter

The third type of novelty filter uses the property of two beam coupling in a photorefractive crystal (7:1029-1031). Figure 4 shows that a weak modulated signal and a strong pump are incident upon a crystal causing an interference pattern to be set up in the crystal with regions of bright and dark fringes. The light and

dark intensity fringes modulates the index of refraction of the crystal. The index modulation then transfers energy from the signal beam to the pump beam due to the electro-optic effect (13:64). The end result is a signal beam that is nearly (or completely) depleted of its energy. For the steady state condition, the constant signal beam and the pump are tightly coupled, nearly depleting the signal beam of its energy. As portions of the signal change, corresponding portions of the holographic grating do not couple the beams as effectively, which temporarily defeats the energy coupling between the two beams. Since the coupling is less efficient, the changing portions of the image are transmitted without depletion.

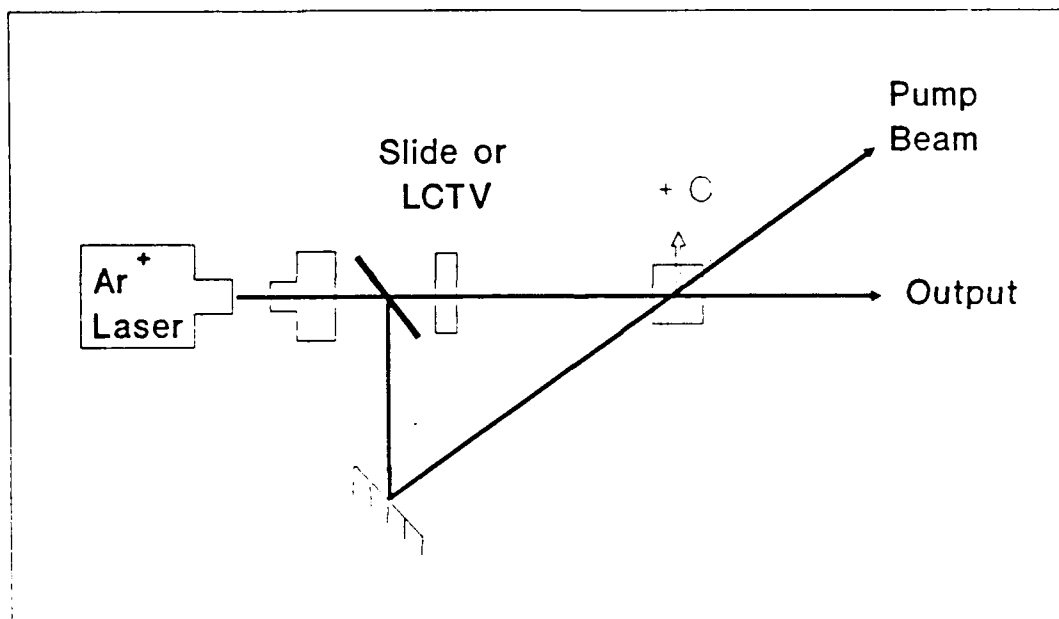


Figure 4. Two-beam coupling novelty filter.

#### 2.4 Optical Image Addition/Subtraction

Previous demonstrations of optical image subtraction and addition have all used a Michelson interferometer configured with a phase-conjugating mirror in place of one the normal mirrors. In the adder/subtractor demonstrated by Chiou *et al* and shown in Figure 5, input images were inserted in each leg. The output signal was extracted from the phase-conjugate beam with two beamsplitters. BS<sub>1</sub> picks off the

subtraction of the two input images (Port A) and  $BS_2$  extracts the addition of the images (Port B) (4:306). This first demonstration of an adder/subtractor required two output ports and does not lend itself to being switchable between addition and subtraction.

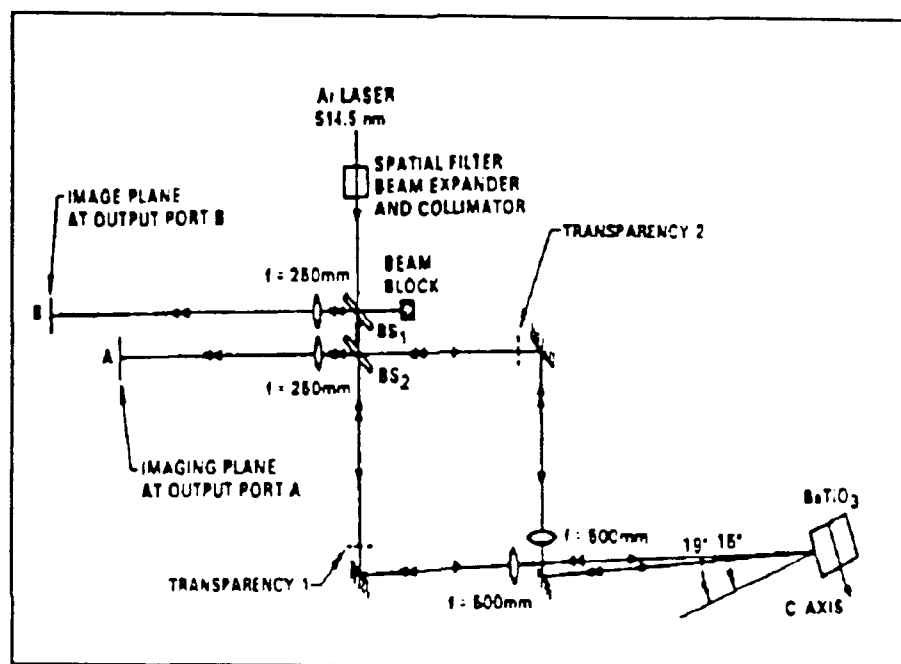


Figure 5. Optical image adder/subtractor with a Michelson interferometer. Port A contains image subtraction and addition is seen output at Port B. (4:306)

In another variation on the technique, Tomita *et al* used the polarization properties of the beams to produce a variable subtractor/adder. In their configuration, which is shown in Figure 6, a linearly polarized wave is divided into two separate beams by a polarizing beamsplitter. The orthogonally polarized beams pass through the images in their respective legs and are conjugated by the crystal. The phase-conjugate signals retrace the paths of their respective legs, recombining at the beam splitter. The output of the beamsplitter then passes through an analyzer at Point A in the figure. By mechanically rotating the analyzer, the output can be changed from image subtraction to image addition (15:425). Being able to vary between addition and subtraction with one output port provided a greater flexibility over the

Chiou design. However, the limiting factor in this design was that the output analyzer was mechanically manipulated. The goal of the research in this thesis was to extend the state of the art one step further and design an electronically switchable adder/subtractor with one output port.

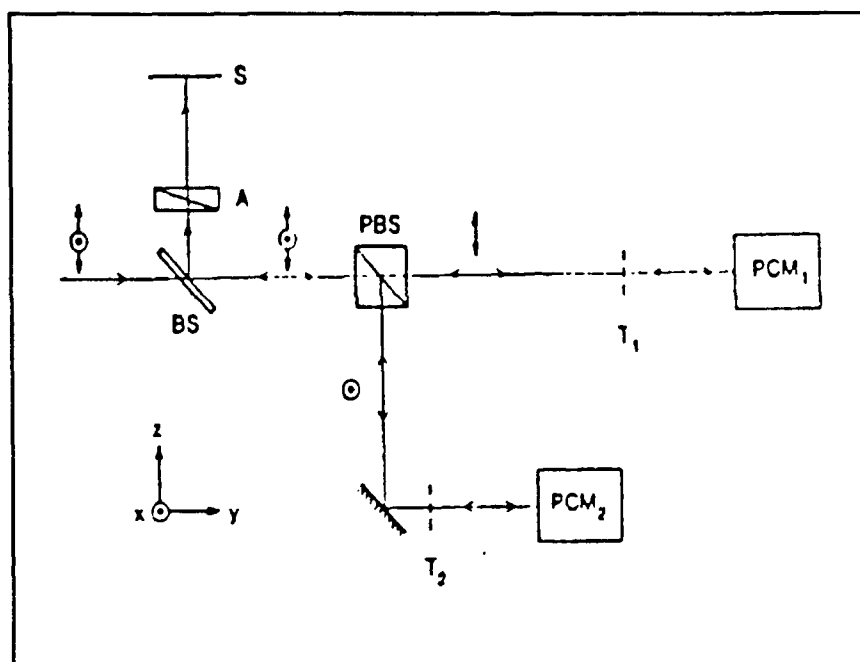


Figure 6. An optical image adder/subtractor using polarization. (15:425)

### III. Materials and Equipment

In this thesis, three BaTiO<sub>3</sub> crystals were used to characterize the beam fanning novelty filter. Table 1 lists the c-axis orientation, crystal sizes and ID #'s used throughout the thesis. The adder/subtractor used crystal 115-F as the phase-conjugating mirror because of its excellent conjugating properties. Each crystal was manufactured by Sanders Associates.

<i>Crystal ID #</i>	<i>Axis Orientation</i>	<i>Crystal Size (mm)</i>
115-F	45°	4.0 x 4.3 x 4.1
119-D	z	6.2 x 3.9 x 5.8
127-K	z	5.2 x 2.5 x 6.0

Table 1. BaTiO<sub>3</sub> crystals used in the thesis.

The laser used throughout the thesis was an 80 mW Argon-ion laser, operating at 514.5 nm. In all the experiments, the laser output was horizontally polarized, spatially filtered and expanded with a Jodon beam expander. A Klinger stepper motor, model # UE72 served as the motion platform when the input object slides had to be moved. The motor can be varied from 0 - 0.4 mm/sec in 0.005 mm/sec increments. The frame grabber used in the experiments was a CID video camera in conjunction with the BeamCode software, developed by Big Sky, Inc. The software had the capability of performing limited data analysis and camera thresholding in addition to capturing images.

## IV. System Parameters Which Characterize Novelty Filters and the Experimental Set-up

### 4.1 Novelty Filter System Parameters

Four parameters were selected to characterize the beam fanning novelty filter. Three of the parameters, spatial resolution, contrast ratio, and onset time, are common parameters used in the field. The velocity response is a new parameter that was developed to describe the movement restrictions for the input image.

**4.1.1 Spatial Resolution.** To determine the spatial resolution of the filter system, the Fourier spectrum of an unfiltered (input) and filtered (output) Air Force (AF) resolution chart were examined. The laser beam passing through the resolution slide was loosely focused onto the crystal as shown in Figure 7. Two beamsplitters were used to examine the Fourier planes of the unfiltered image, before the crystal.

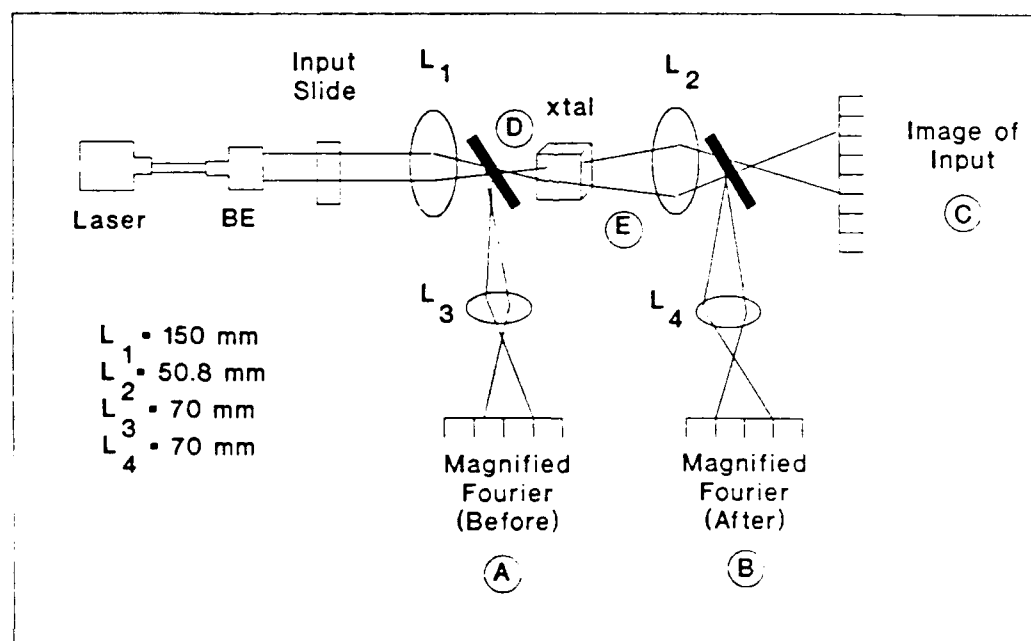


Figure 7. Experimental set-up to examine the spatial resolution of a beam fanning novelty filter.

and the filtered output, after the crystal. The Fourier planes were digitally captured by a CID camera and analyzed using the BeamCode software. Two sinusoidal computer generated holograms with known spatial frequencies were used to calibrate the captured Fourier planes. The methodology used to produce the computer generated holograms is discussed in Appendix B.

*4.1.2 Contrast Ratio.* Moving and stationary output images were digitally captured so that the contrast ratio between the brightest enhanced portion of the image and the brightest stationary background could be calculated using:

$$C = \frac{I_{max} - I_{min}}{I_{max}} \quad (3)$$

where

- $C$  = Contrast ratio
- $I_{max}$  = Maximum intensity of the filter with an object moving
- $I_{min}$  = Maximum intensity of the filter output with the input object stationary

As a figure of merit, an ideal novelty filter would have a ratio of  $C = 100\%$ . Ratios as high as 93% have been achieved by Anderson *et al* using a Pockels Cell as a single pixel image (1:124).

*4.1.3 Onset Time.* Immediately after an image is first presented at the input of a novelty filter, the entire image will be passed since everything in the scene is initially novel. Over a short period of time, however, the crystal adapts to the new scene, and the stagnant portions of the image begin to fade from the output, until a steady state is reached (assuming nothing else in the scene changes). The onset time of the filter,  $\tau_{filter}$ , is defined as the 1/e point of this decay. To measure  $\tau_{filter}$ , a strip chart recorder, attached to an intensity detector, will record the exponential decay of a novel input signal.

4.1.4 *Velocity Response of the Crystal.* The velocity response of the crystal determines the detectable minimum and maximum velocity of an object moving across the input image. Anderson *et al* have achieved velocities as high as 0.25 mm/sec (2:646). To determine the minimum and maximum velocity for each crystal, an AF resolution chart was set into motion across the expanded laser beam. The velocity of the hologram was decreased and increased to find the minimum and maximum values, respectively for each crystal. A velocity limit is defined as the speed of an object when there is no longer an output from the filter. For a video scene of a battlefield, this velocity can be scaled up to an actual velocity of a real object based on the range of the object to the camera and the field of view of the camera. For example, consider a scenario with the following parameters and shown in Figure 8: Camera FOV =  $\pm 15^\circ$ , Object Speed = 100 km/hr, Object Range: 5 km. Modulator transverse dimension = 5 cm. Using these parameters, the object's speed

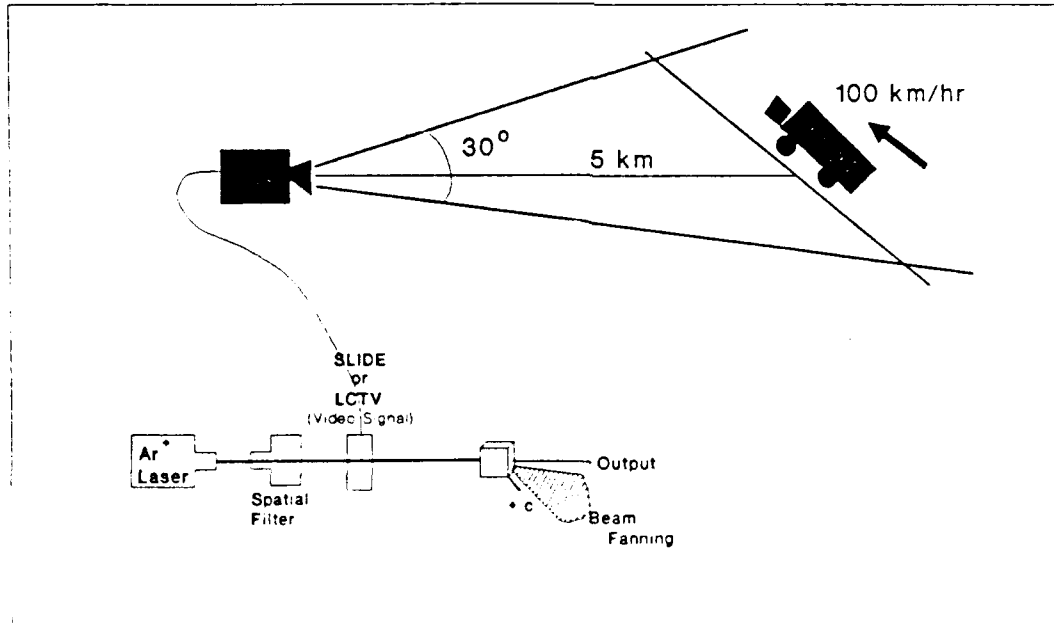


Figure 8. Scenario relating an object's transverse speed in the real world to the input plane of reference of a novelty filter. In this case, an object moving at 100 km/hr translates to 0.52 mm/sec in the input plane.



in the real world plane of reference would translate to 0.52 mm/sec in the input plane of reference of the novelty filter. This value can be compared with the experimental results to be discussed in the next chapter.

## 4.2 *Beam Fanning Experimental Set-up*

**4.2.1 Spatial Resolution.** Figure 9 shows the experimental set-up used to measure the spatial resolution achievable using the three crystals. The input image was reduced by a factor of 0.3 and imaged onto each crystal. Each of the crystals were oriented such that the minified image intersected the c-axis at approximately  $45^\circ$ , so that the gain would be optimized. This size reduction was suitable for crystals 115-F and 119-D since the image size was smaller than the crystal faces. Crystal 127-K had a smaller face which required a stronger demagnification of the input. In this case a demagnification of 0.1 with  $L_1 = 50.2$  mm was sufficient for data collection.

The camera was placed at Points A and B in Figure 9 such that the intense DC component was just outside the field of view of the camera. Since the less intense high frequency components were the items of interest, placing the camera to one side of the DC allowed those components to be captured. The input image was set in motion with a Klinger stepper motor, model #UE72.

**4.2.2 Contrast Ratio.** To calculate the contrast ratio, images were captured with the camera placed at Point C in Figure 9 with the image moving across the expanded beam and after the steady state was achieved with the object stationary. The BeamCode frame grabber software can be used to measure  $I_{max}$  and  $I_{min}$  so that the contrast ratio,  $C$ , can be calculated.

**4.2.3 Onset Time** The set-up in Figure 9 was also used to determine the onset time,  $\tau_{filter}$ , of each crystal. A power detector was placed at Point D to measure the incident power going into the crystal and at Point E to measure the exponential decay as the filter responds to the input image. The laser output power

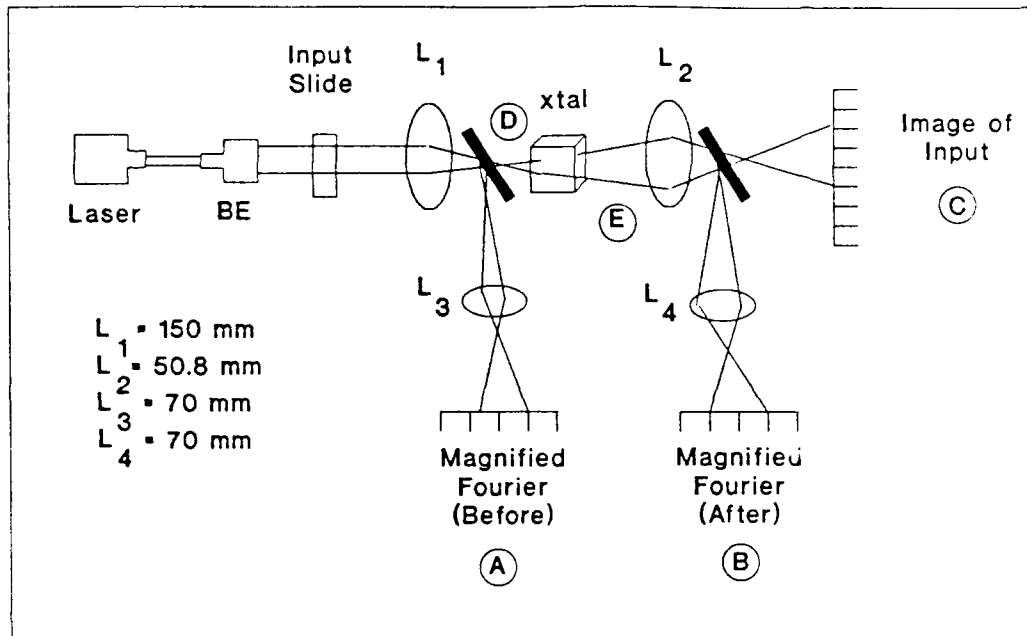


Figure 9. Experimental set-up to examine the spatial resolution limit of the beam fanning novelty filter.

was varied so that at least five data points could be taken. A strip chart recorder was attached to the detector at Point E to plot the response so that the  $1/e$  time could be measured. The experimental procedure and a sample calculation are discussed in Appendix C.

**4.2.4 Velocity Response.** The same set-up shown in Figure 9 was used to determine the velocity response of each crystal. The camera was placed at Point C and the Klinger stepper motor speed was varied to determine the slowest and fastest speeds of the object such that the filter would not respond and no output occurred.

## V. Beam Fanning Novelty Filter Results and Discussion

### 5.1 Spatial Resolution

Figure 10 shows the results of the spatial resolution experiments. Pictured in the figure is half the Fourier plane for an unfiltered AF resolution chart, (a), and filtered charts for each crystal, (b)-(d). In pictures (b)-(d), the AF chart was moving to the right at 0.4 mm/sec, the maximum limit of the stepping motor. Not shown in the figure are two sinusoidal computer generated holograms of known spatial frequencies of 5.16 and 2.48 cyc/mm that were used to establish a conversion factor to convert linear distance of Figure 10 in the x-direction to a spatial frequency scale in cyc/mm. Table 2 shows the highest horizontal spatial frequency obtained for each of the images pictured in Figure 10.

It is apparent from the data in Figure 10 and Table 2 that both the 45°-cut crystal, #115-F, and the thick z-cut crystal, #119-D, have the best absolute spatial resolution. The thin crystal, #127-K, lacks both high frequency definition and overall intensity of frequency components resulting in poor image resolution.

It is also clear that each filter, regardless of the crystal size or structure, acts as a high pass filter, as previously reported by Anderson *et al* (2:635). In other words, the novelty filter acts as an edge enhancer. The edge enhancement can be accentuated by placing the Fourier plane onto the crystal face instead of imaging

	<i>Unfiltered Image</i>	<i>Crystal # 115-F</i>	<i>Crystal # 119-D</i>	<i>Crystal # 127-K</i>
<i>Spatial Resolution (cyc/mm)</i>	50	45	44	18

Table 2. Highest spatial frequencies obtained from an unfiltered and filtered AF resolution chart using a beam fanning novelty filter.

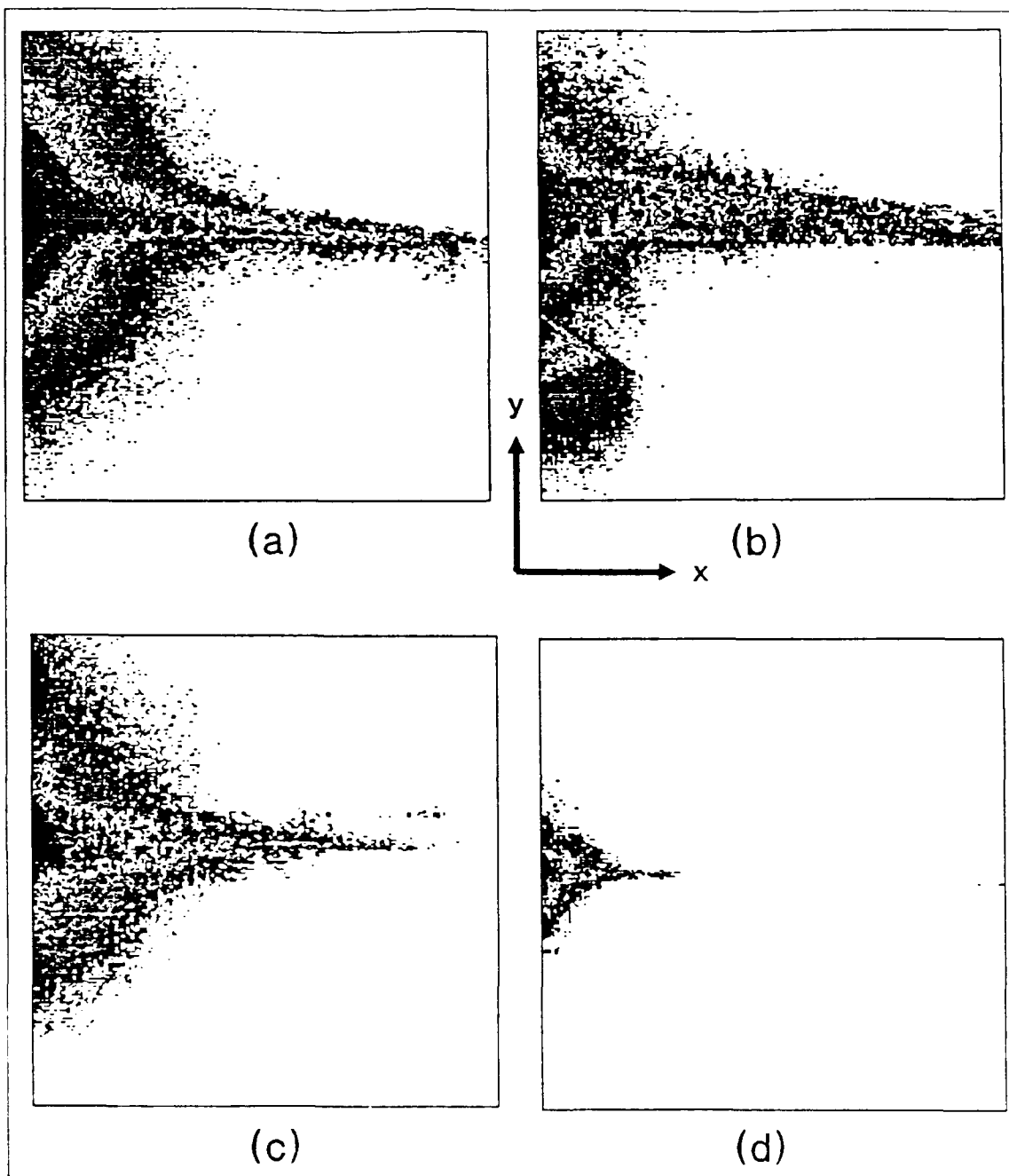


Figure 10. Fourier spectrums of an AF resolution chart using a beam fanning novelty filter. (a) Unfiltered spectrum. (b) Spectrum after being filtered by Crystal 115- F. (c) Spectrum filtered by Crystal 119-D. (d) Spectrum filtered by Crystal 127-K.

a reduced version of the input image onto the face. In this case, the intense low frequency components fan first and therefore are filtered quickly whereas the less intense high frequency components pass through nearly unattenuated. Since the filter life time is much longer for low intensity components, as will be discussed in Section 5.3, the edges remain visible for a longer period of time. In contrast, placing a reduced image onto the crystal allows a more uniform filtering to occur. Imaging spreads the energy more evenly over the crystal face rather than being concentrated in one spot as with the Fourier plane. This phenomenon was also reported by Ford *et al* (11:858).

## 5.2 Contrast Ratio

Figure 11 shows the experimental results obtained during the measurement of the contrast ratio,  $C$ , of all three crystals as the incident power was increased from 1 mW to 25 mW. Each crystal was positioned in the image plane of a miniified AF resolution chart with its c-axis at  $45^\circ$  to the image plane. Two output images were captured, one while the AF chart is moving and the second after the steady state condition was obtained with the object stationary. Capturing a filtered output while the object is stationary provides the amount of intensity that *leaks* through the filter after the steady state condition is achieved. Ideally, this value would be zero, however, there is a limit in each crystal as to how much intensity it can filter.

Figure 11 clearly shows that the contrast ratio,  $C$ , quickly erodes as the incident power is increased. The best ratios are in the 1-3 mW range. Not shown in the figure are the trends of the two intensities that make up the ratio. It should be noted that even though  $I_{max}$  fluctuated as much as 50% of its maximum value, it is  $I_{min}$  that is the dominating factor in driving down the contrast ratio at the higher intensity levels. For example,  $I_{min}$  increased to more than twice its original value for crystal 115-F as the incident power on the crystal was increased from 1 mW to 24 mW. This leads to the conclusion that the crystal's ability to fully fan the input during

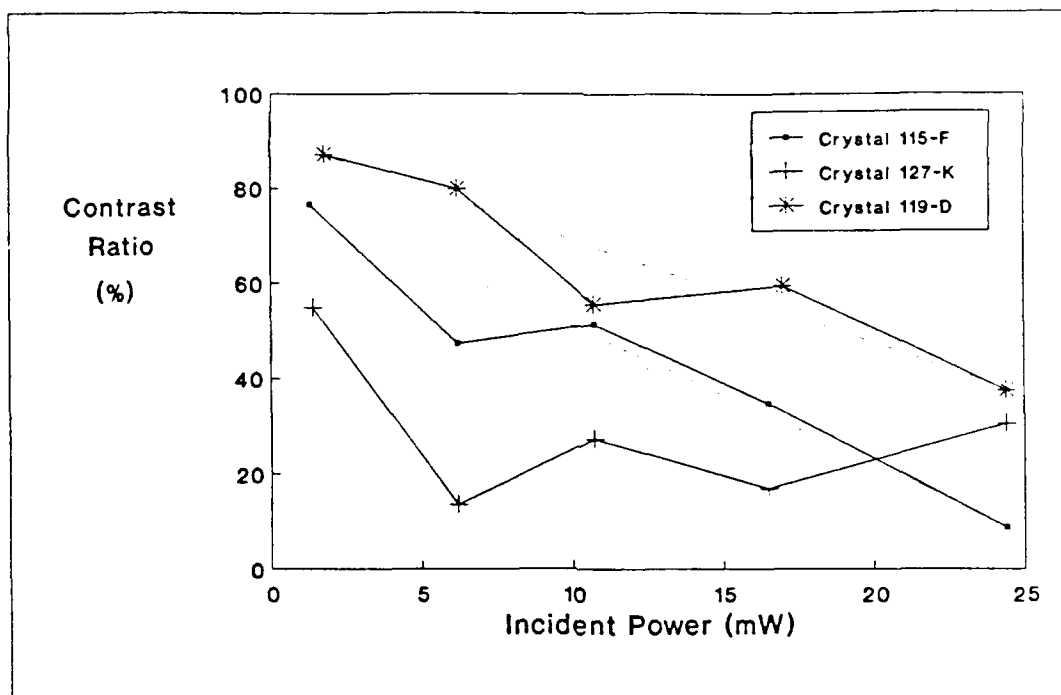


Figure 11. Experimental results for the Contrast Ratio,  $C$ . The dotted line represents a linear interpolation of the curves.

the steady state condition is breaking down at higher power levels. The filter no longer sufficiently blocks the intense background and therefore  $I_{min}$  increases and  $C$  decreases.

The highest (best) contrast ratio was achieved with the thick z-cut crystal, # 119-D, with  $C \approx 87\%$ . The  $45^\circ$ - cut crystal followed closely with a maximum ratio of  $C \approx 77\%$ . These two curves also have approximately the same slope if linearly interpolated which indicates a relationship for the  $BaTiO_3$  material. In other words, the two curves for crystals 115-F and 119-D are decaying at approximately the same rate. The rate is represented by the slope of the linearly interpolated line. Therefore, if a contrast ratio and its corresponding incident power level is known for any  $BaTiO_3$  crystal, the contrast ratio response for that crystal for a range of incident power levels can be easily estimated by using the simple line equation,  $y = mx + b$ . This conclusion provides a simple, but effective technique for modeling the contrast ratio. Unfortunately, the thin crystal showed consistently poor results

in the spatial resolution experiment and this experiment and was not used in drawing this conclusion concerning the linearity of the material.

### 5.3 Onset Time

Figure 12 shows onset times,  $\tau_{filter}$ , for each of the three crystals as the incident power was varied from  $\sim 1.0$  mW to  $\sim 35$  mW. Crystal 115-F had the overall fastest time. The thin crystal, # 127-K, was almost as fast as # 115-F, but it began to show an unusual behavior at high powers. As the power was increased above 26 mW, crystal 127-K showed an initial exponential decay to the half power point and then a slight rise followed by a slower decay as shown in Figure 13. This unusual response was very different from a normal exponential decay exhibited by the other two crystals. Crystals 115-F and 119-D both showed a smooth, consistent exponential decay with a single time constant. An example of a typical response is shown in Figure 24 in Appendix C. It was not determined in this thesis the exact mechanism causing this phenomenon. However, coupled with the poor results in the previous two experiments, these results indicate defects in both the crystal material and structure.

Crystal 119-D had the longest onset time of the three crystals. This was expected since the propagation distance within the crystal is  $\sim 6.2$  mm as opposed to 5.2 mm for # 127-K and 4.0 mm for # 115-F. According to Pepper *et al*, the beam fanning phenomenon is related to the number of charge carriers present within the crystal (13:64). With a longer propagation distance, there are more mobile carriers to move, and therefore, a longer onset time for the filter. In addition, # 119-D is also a z-cut crystal and therefore access to the peak gain is hindered, even when oriented at  $45^\circ$  as opposed to the  $45^\circ$ -cut crystal with normal incidence, as explained in Chapter II. It is predicted that this crystal will also have a low velocity response since its  $\tau_{filter}$  is low. Since this crystal requires more time to achieve the steady state condition, the index grating will be written slower resulting in a lower minimum

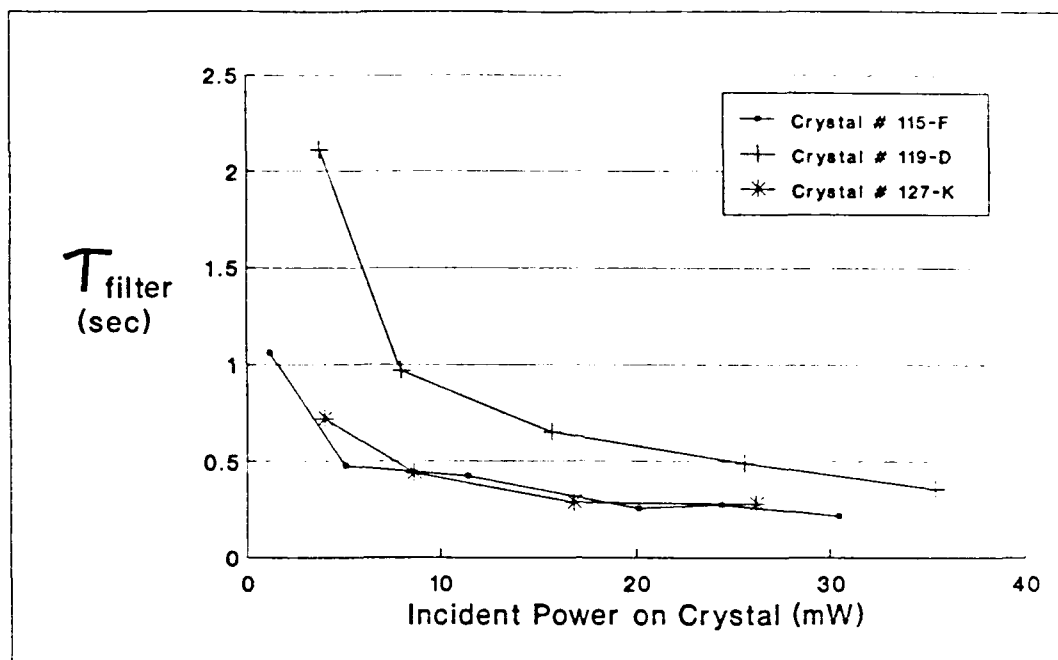


Figure 12. Experimental results for the Onset Time experiments.

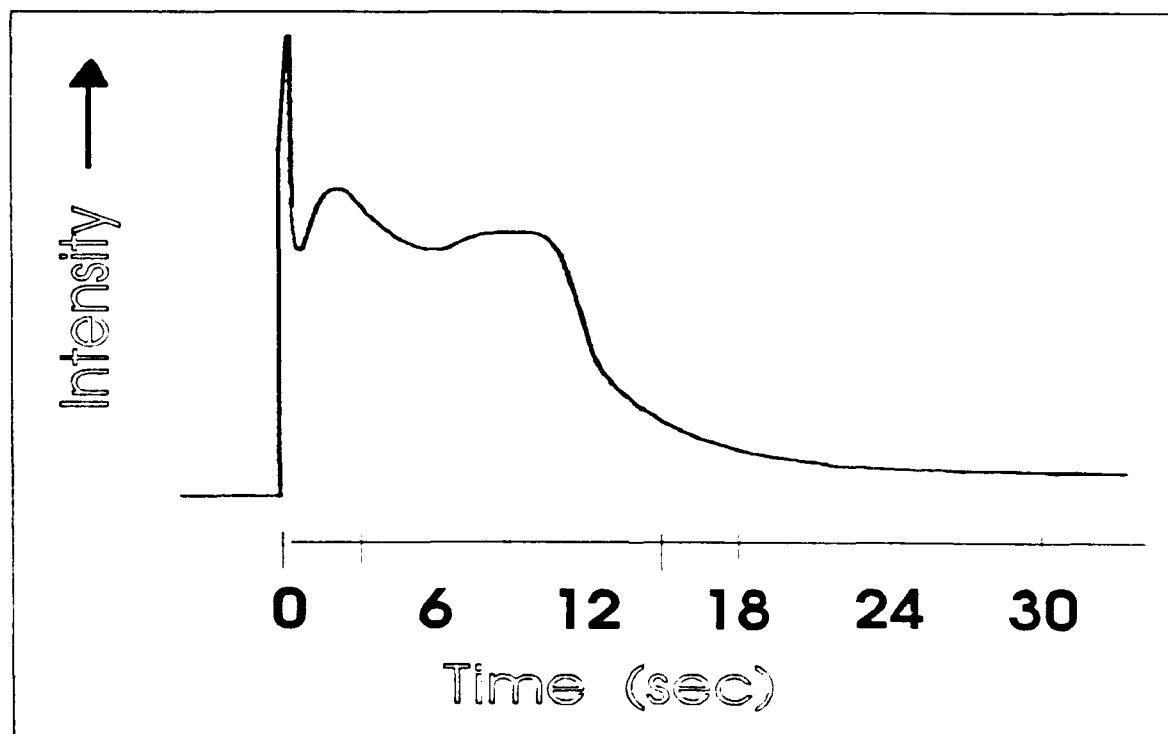


Figure 13. Unexplained onset behavior of crystal 127-K at powers greater than 26 mW.



velocity to prevent an output of the filter (see Section 5.4).

This difference in onset times for the z- and 45°-cut crystals begins to diminish as the incident power is increased, as shown in Figure 12. At powers greater than 30 mW, the onset time of the 45°-cut crystal reaches a plateau at approximately 0.3 sec. However, in both the z-cut crystals the onset times continued to decrease, with crystal # 119-D approaching 0.5 sec at 36 mW. Most likely at higher powers, ( $\gg$  40 mW), the number of crystal mobile carriers becomes saturated and all the carriers are moving and thus the onset times level off to a constant value as discussed by Pepper (13:64). Therefore, if Figure 12 were expanded off the right side of the page, the expected result would be three curves flattening off to three steady state values; 0.3 sec for # 115-F, 0.4 sec for # 119-D, and 0.25 sec for # 127-K.

The special 45°-cut crystal had the shortest, most consistent onset time; whereas crystal 119-D had the greatest variation as the incident power is increased. The consistently quick response of # 115-F makes it the best choice for detecting *relatively* fast objects regardless of the incident power. The term *relatively* is stressed here since the onset time of the crystal is based on the speed of an object moving in the *input image plane of reference* and not in the real world plane of reference. A fast onset time is necessary in order to filter out the ghost that trails behind the moving object. An example is shown in Figure 14 which shows an output of the filter as an object "T" moved to the right followed closely by its ghost. The ghost occurs at the previous position of the object as seen by the crystal. If the crystal has a fast  $\tau_{filter}$ , the ghost will quickly fade as the crystal attempts to attain a steady state condition. Suppressing the ghost causes a higher resolution since only one object is present rather than the object plus its trailing ghost, which causes a blurring effect to the eye. As was seen in Section 5.1, crystal 115-F also had the highest spatial resolution.

On the other hand, a variable onset time, like that demonstrated by # 119-D, also has its advantages when  $\tau_{filter}$  can be tuned by adjusting the input power. A

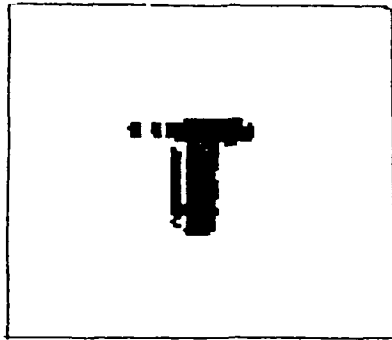


Figure 14. A filtered output of a "T" as it moved to the right followed closely by its ghost.

brighter trail, and thus a history of the motion of a moving object, can be obtained. The spatial resolution would in turn decrease, but the streaking nature of a *time elapsed* snapshot of the moving object could help in locating and tracing moving objects.

The thin crystal, # 127-K, could offer the speed of a 45°-cut crystal without the added expense of fabricating a z-cut. However, the irregular performance at higher powers, as shown in Figure 13, may preclude this particular crystal from becoming a good novelty filter candidate.

#### 5.4 Velocity Response

Shown in Figure 15 are the velocity response curves showing the minimum velocities detectable for each crystal as the power was increased from 1 mW to 25 mW. Maximum speeds were unattainable due to the limitations of the stepper motor used (the maximum velocity of the stepper motor was 0.4 mm/sec which was still

within the upper response range of the crystal, i.e. at the maximum speed there was still a well defined output from the filter). Even the minimum velocity for crystal 127-K was greater than the stepper motor capacity beyond 17 mW, as shown in the figure. A motion platform with a range greater than 3.0 mm/sec is recommended.

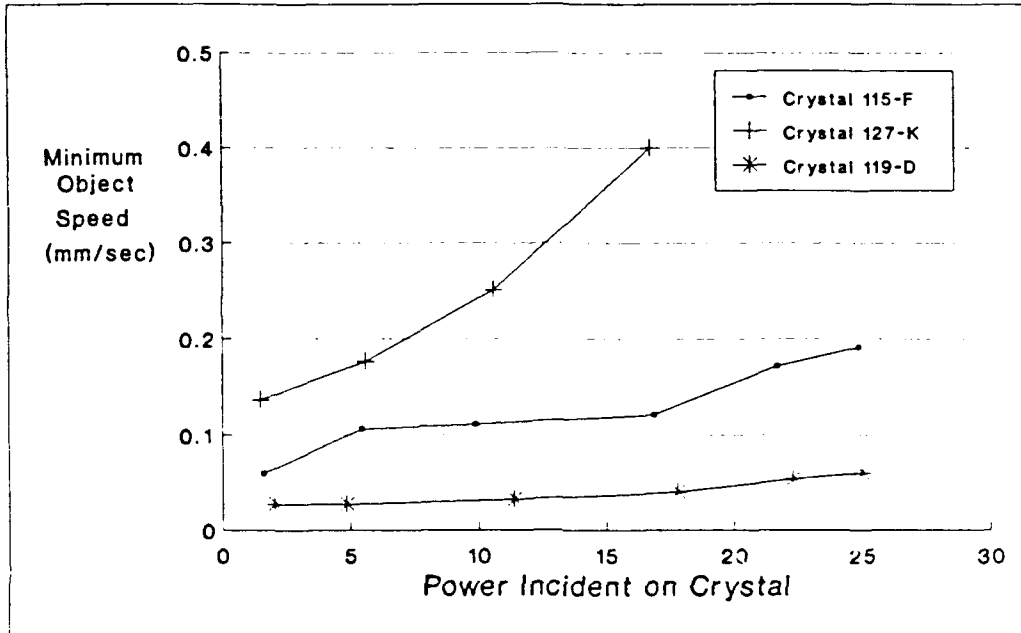


Figure 15. Minimum velocities for each of the three crystals. Maximum velocities were unattainable due to the limitation of the stepper motor.

This was a value obtained in an uncontrolled experiment by manually moving the object at different rates. The stepper motor was sufficient, however, to find minimum object velocities shown in the figure.

Crystal 119-D showed the most stable and slowest minimum velocities for the intensity range used in the experiment. The slow velocity was predicted from the  $\tau_{filter}$  measurements in Section 5.3, since that crystal has the longest onset time, approximately 2 sec. With a long  $\tau_{filter}$ , the input object needs only to move at a slow rate to cause an output of its image and ghost image, since the filter requires a relatively long time to reach the steady state. As mentioned previously in Section 5.3, this crystal would be excellent for tracking objects, including extremely slow objects due to its low minimum velocity response and long  $\tau_{filter}$ .

The 45°-cut crystal also shows a relatively stable minimum velocity throughout the experimental intensity range. Coupled with its fast  $\tau_{filter}$ , as shown in Figure 12, this crystal is excellent for filtering a wide band of velocities, with the band remaining constant over a wide range of input intensities. In contrast, the thin crystal, # 127-K, showed the most erratic behavior, exhibiting a parabolic response in minimum velocity. Since its  $\tau_{filter}$  response is nearly the same as crystal 115-F (see Figure 12), it is expected that the maximum velocities for these two crystals would be closely matched. [Note: The maximum velocity that the crystal responds to is closely related to the onset time of the filter; as  $\tau_{filter}$  decreases (faster), the maximum velocity increases.] Therefore, by changing the input intensity on the thin crystal, a selective velocity range could be tailored to a narrower band than with the 45°-cut crystal.

## VI. Switchable Optical Adder/Subtractor: Theoretical Analysis and Experimental Set-up

The system described in this section relies on coherent destructive interference between two signal beams for image subtraction and incoherent addition of images for image addition. The experimental setup shown in Figure 16 is based on a Michelson interferometer. The interferometer has been modified by using a phase conjugating mirror (PCM), two electro-optic crystals, and two polarizing beam splitters in one of the legs of the interferometer. This is a variation of the image subtractor described by Chiou, *et al* (4:306-308)(5:385-392).

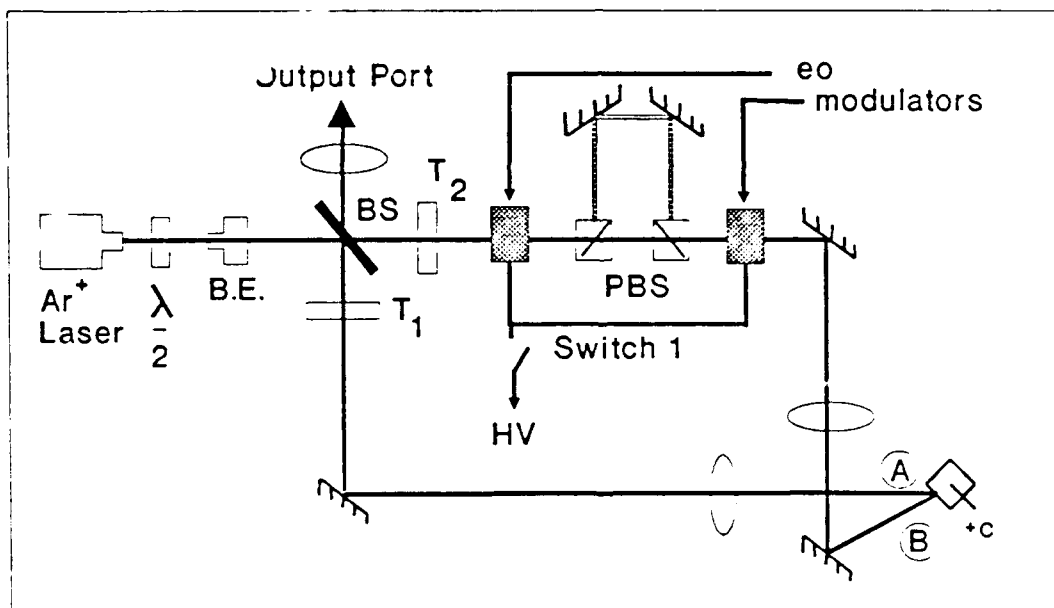


Figure 16. Schematic diagram of the switchable optical image adder/subtractor designed in the thesis.

For image subtraction, Switch 1 is left open which leaves the two e-o crystals unbiased so that horizontally polarized light passes through unaltered. Light originating from the laser and reaching point A in Figure 16 will have an amplitude of  $(rEt_1)$  before reaching the PCM, where  $r$  is the reflectance of the beam splitter (BS)

from left to right,  $E$  is the amplitude of the original laser beam, and  $t_1$  is the amplitude transmission coefficient of the first object. Upon being phase conjugated, the beam will retrace its phase front, becoming  $(t\rho r^* E^* T_1)$  at the output port after the beam splitter, where  $T_1 = |t_1|^2$  and  $t$  and  $\rho$  are the beam splitter transmittance and PCM reflectivity, respectively. The beam tracing through the upper leg of the interferometer passes through the first e-o crystal, retaining its horizontal polarization, is transmitted by the two polarizing beam splitters and transmitted through the second e-o crystal, again unaltered. At point B, just before the PCM, the amplitude of this beam is  $(tEt_2)$ , assuming that the losses in the e-o crystals and polarizing beam splitters are neglected. After being conjugated and retracing back through the beam splitter, the amplitude of the upper leg is  $(r'\rho t^* E^* T_2)$ , where  $r'$  is the reflectance of the beam splitter from right to left. At the output port, just after the beam splitter, the two beams recombine. Since each beam has been phase conjugated and the path length difference is within the coherence length of the Ar-ion laser ( $\sim 3$  cm), the two beams are mutually coherent and add coherently:

$$I_{out} = |t\rho r^* E^* T_1 + r'\rho t^* E^* T_2|^2 \quad (4)$$

The use of the Stokes relations (12:242):

$$rr^* + tt'^* = 1 \quad (5)$$

$$r^*t + t^*r' = 0 \quad (6)$$

allows the reduction of Equation (4) to:

$$I_{out} = RT |\rho E^*|^2 |T_2 - T_1|^2 \quad (7)$$

where  $R = |r^*|^2$  and  $T = |t|^2$ , as was shown previously by Chiou *et al* (4:306). Equation (7), above, shows that the resultant intensity of the output image is proportional

to the square of the difference of the two input images.

To obtain image addition, Switch 1 is activated so as to bias the crystals with a  $\lambda/2$  voltage, which rotates the polarization  $90^\circ$ . This effect causes the polarizing beam splitters to divert the light into an extra length chosen to extend well beyond the coherence length of the laser beam. Light re-enters the interferometer where its original polarization is restored by the second e-o crystal, suitable for self-pumped phase-conjugation in the BaTiO<sub>3</sub> crystal. Light in the lower leg travels the exact same path described for image subtraction. However, since the upper leg was *delayed* outside the coherence length of the laser, the return beam in the upper leg is no longer mutually coherent with that in the lower leg. With the two beams being incoherent, their intensities add, yielding the addition of the two input image intensities:

$$\begin{aligned} I_{out} &= |t\rho r^* E^* T_1|^2 + |r' \rho t^* E^* T_2|^2 \\ &= RT |\rho E^*|^2 [T_1^2 + T_2^2] \end{aligned} \quad (8)$$

This technique allows the output to be easily switched between addition and subtraction. It should be noted, however, that the subtraction is actually an absolute value subtraction, as described by Equation (7). Therefore, the operation 1-0 and 0-1 yeild the same result of 1 instead of 1 and -1, respectively.

## VII. Switchable Adder/Subtractor Results and Discussion

Two experiments were conducted on the adder/subtractor, shown in Figure 16, to evaluate its capability to properly coherently subtract two images and incoherently add them, as described by Equations (7) and (8), respectively. Both experiments were conducted with the 45°-cut BaTiO<sub>3</sub> crystal, # 115-F, as the PCM. The specially cut crystal was oriented for maximum self-pumped phase-conjugation by both legs of the interferometer, ~25° to the c-axis. For image subtraction, the mirrors in both legs were adjusted such that the two beams were incident on the crystal at the same point, overlapping one another. An alternate method for producing phase-conjugate beams would be to have the two beams mutually pump the crystal (16:16-21). Each of these two methods were tested and both produced a proper phase-conjugate beam. Since there was no noticeable difference between the two methods, the first method was chosen for the adder/subtractor.

When the system was switched to image addition, the mirrors in the adjustable length leg and the polarizing beamsplitters were adjusted such that the two beams incident on the crystal did not overlap. It was noticed that the legs conjugated more efficiently when the beams did not overlap during image addition.

In the first experiment, the transparencies  $t_1$  and  $t_2$ , were removed, which represents two images with  $t_1 = t_2 = 1$ . The interferometer output was detected using a power meter connected to a strip chart recorder. The chart recorder trace is shown in Figure 17. At the starting point of the recording, on the right end of the trace, the beams in both legs of the interferometer are blocked, i.e.,  $T_1 = |t_1|^2 = T_2 = |t_2|^2 = 0$ . The output shows the zero detected by the power meter [0-0=0]. In Step (a), the beam in the lower leg was unblocked, implementing a  $T_1 = |t_1|^2 = 1$  and  $T_2 = 0$  state. Thus, the level of the output represents the power of the beam in the lower leg, corresponding to an algebraic operation [1-0=1]. In Step (b), the beams in both legs are unblocked, i.e.,  $T_1 = T_2 = 1$ , with Switch 1 open. In this



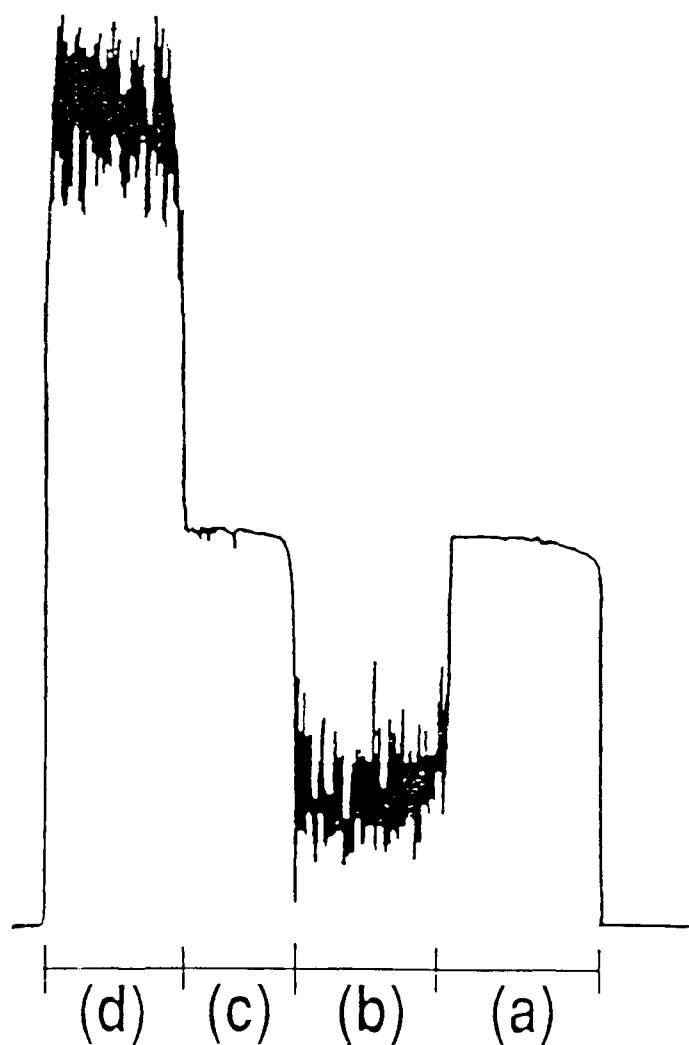


Figure 17. Intensity detected at the output port of the switchable adder/subtractor. (a) Lower leg full intensity, (b) Image subtraction, (c) Upper leg full intensity. (d) Image addition.

state, the interferometer acts as a subtractor, and produces an output corresponding to  $[1-1=0]$ . The subtraction is coherent subtraction and is susceptible to table and air vibrations as shown by the modulated subtraction level. However, regardless of the noise, the output in this state is still well below 50% of the original level in Step (a), yielding an accurate subtraction of the two one-dimensional images. When the beam in the lower leg is blocked in Step (c), which implements  $T_1 = 0$  and  $T_2 = 1$ , the output is increased to a level comparable to that in Step (a) according to the operation  $[0-1=1]$ . Finally, in Step (d), the beams are unblocked and Switch 1 is closed, causing the upper leg beam to be diverted through the extra length. For this case, the interferometer acts as an adder in accordance with  $[1+1=2]$  and the output is seen to be nearly two times that in Step (c). The modulation seen in Step (d) is similar to that in Step (c) and may be due to light leaking through the polarizing beam splitters and causing coherent image subtraction. The leak in the polarizing beam splitters is due to the e-o crystals not rotating the light to a perfect vertical polarization which is needed to divert the light into the extra length for addition. However, even with the small modulation on top of the addition, the average is still well above the original levels in Steps (a) or (c). Therefore, with appropriate thresholding on a detector, image subtraction and addition can be achieved using this technique.

In the second experiment, two images were used to demonstrate the capability of the system to process two-dimensional images. In this experiment,  $t_1$  was a square and  $t_2$  was a circle. The results are shown in Figure 18. Figure 18a is the difference of the two images when Switch 1 is open, allowing for coherent destructive interference at the output port, as seen by the dark region where the circle overlaps the square. In the overlapping region the equal intensities from the circle and square destructively interfere to produce the dark area. The subtraction can also be seen in the cross-sectional profile in (b). When Switch 1 is turned on, causing light to be diverted through the extra length, the sum of the two images is obtained as shown

in Figure 18c. Here the overlapping region is now approximately two times brighter than the remainder of the images as shown by the addition cross-sectional profile in (d).

These experiments successfully demonstrated the ability of the switchable optical adder/subtractor to properly add and subtract two images in a switchable configuration. This type of device offers considerable flexibility in performing optical computing and matrix algebra, as well as optical image processing, all under the control of a computer.

This device has many potential industrial and military applications as well as scientific uses. By placing a reference image in one leg and a spatial light modulator in the other, various forms of quality control can be performed on mass production assembly lines. Various modulators are applicable to the adder/subtractor. The least expensive modulator could be a LCTV. If more resolution is required, magneto-optic and liquid crystal light-valve modulators can also be used but at a higher cost. Military applications include, optically adding aircraft and situation awareness information to the outside scene in head-up displays (HUDs), target tracking, image segmentation, and target recognition pre/post processing in subsystems.

In addition, the parallel nature of this addition and subtraction operation offers increased speed over its electronic serial counterparts. It should be noted that the overall speed of the system is limited by the phase conjugating mirror, the switching response of the e-o crystals and any sort of image input device (LCTV) and not by the algebraic nonlinear interferometry operation of the light.

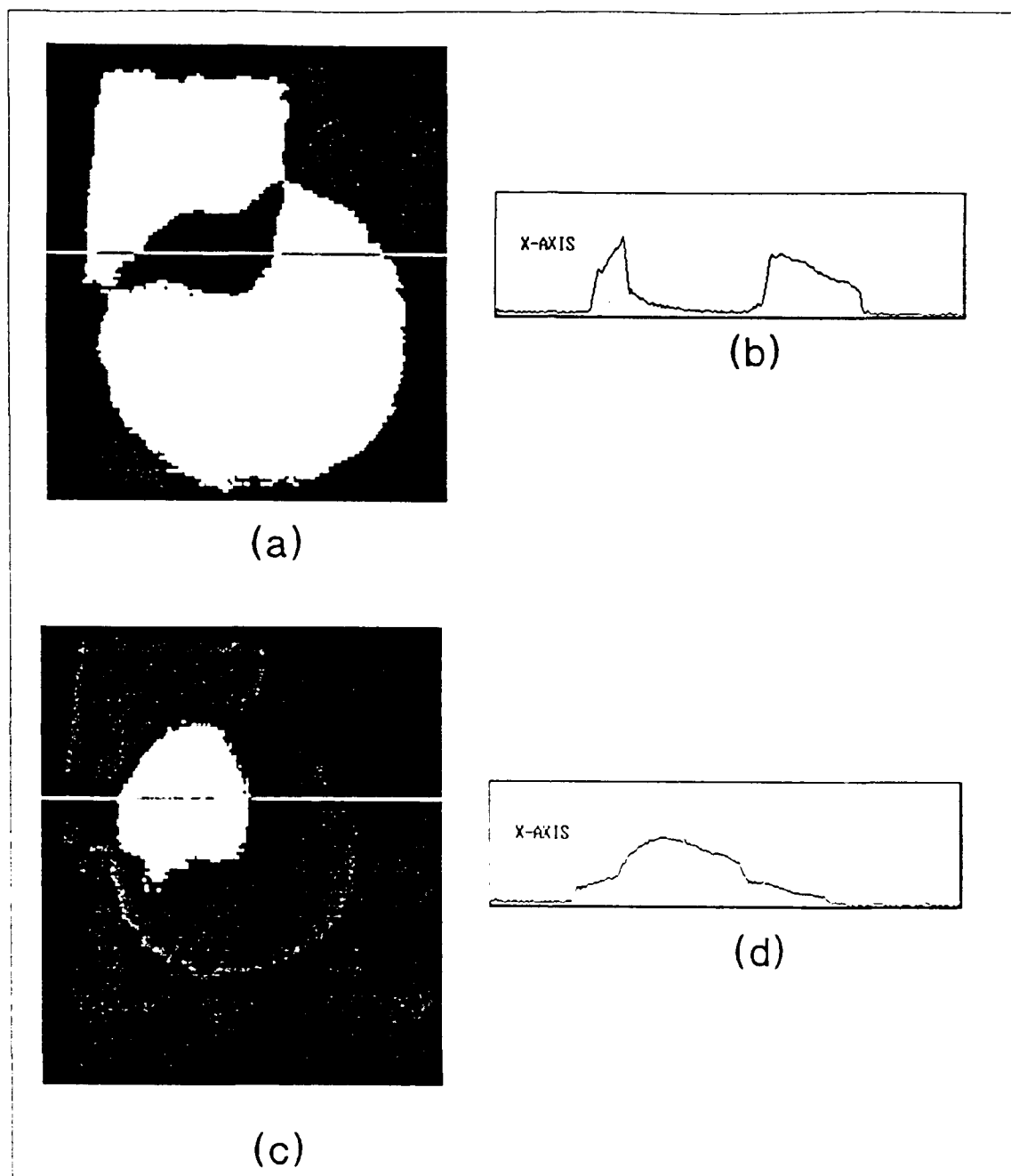


Figure 18. Optical image addition and subtraction. (a) A circle and square are subtracted when Switch 1 is open. (b) cross-sectional profile showing the subtraction, (c) image addition with Switch 1 closed. (d) cross-sectional profile showing addition.

## VIII. Conclusions & Recommendations

### 8.1 Beam Fanning Novelty Filter

This thesis research successfully characterized the beam fanning configuration for novelty filtering using both z-cut and 45°-cut BaTiO<sub>3</sub> crystals. The research determined trends and relationships among the four filter characteristics defined in Chapter IV. These characteristics are qualitatively summarized in Table 3. One

<i>Crystal ID #</i>	<i>Spatial Resolution</i>	<i>C</i>	$\tau_{filter}$	<i>Minimum Velocity</i>
#115-F	Excellent	Good (linear)	Quickest (flat)	Slow (flat)
#119-D	Good	Excellent (linear)	Slow (variable)	Slowest (flat)
#127-K	Poor	Poor (irregular)	Quick (flat)	Variable

Table 3. Qualitative summary of the beam fanning novelty filter portion of the thesis.

important quality not depicted in the table, is the simplicity of the beam fanning configuration as opposed to the Michelson interferometer or two-wave mixing techniques. Those two techniques require greater beam control and alignment and are more susceptible to vibration than the beam fanning technique.

Based on the results given in Table 3, the beam fanning filter can be tailored to different military applications. For example, if the system designer requires a filter with high spatial resolution, high contrast ratio, low laser power, and broad band velocity selection, then the 45°-cut crystal would be the most logical choice. On the other hand, the thick crystal could be used to track moving objects, creating a ghost that trails the object for efficient locating and tracking. The idea of a velocity

analyzer, synonymous to a spectrum analyzer, could be supported by the thin crystal which has a variable minimum velocity by adjusting the input intensity.

The beam fanning novelty filter would also be applicable to an intrusion alarm or surveillance system. For example, a low light TV (LLTV) or an infrared camera could be used as the remote sensing device. Initially, the entire scene from the camera is novel and will be passed by the filter. However, after the filter has reached its steady state condition, only moving objects in the field of view of the camera will cause an output to the filter system. A simple intensity detector at the output port could then be used as the triggering mechanism to set off an alarm or alert authorities. The detector would sense the high intensity of moving objects being passed by the filter.

It is strongly recommended, however, that prior to applying the beam fanning novelty filter to applications mentioned above, additional research be performed on additional novelty filter configurations as well as additional crystals in the beam fanning configuration. Additional novelty filter configurations and crystals will provide the system designer with a more complete synopsis of novelty filtering and other options that may not have appeared in the experiments performed in this thesis research.

In addition, it is recommended that a liquid crystal TV (LCTV) replace the moving slide used in this thesis. The LCTV can be used as either an amplitude modulator (equivalent to the slides) or as a polarization modulator (2:640-642). Using a second type of modulation, other than amplitude modulation, could provide a more complete characterization of the beam fanning novelty filter. The LCTV also offers the convenience of replaying a standardized video tape of a moving object, providing more control over the experimental parameters, and thus increasing the repeatability of the experiments. An LCTV would also offer a wider range of object velocities than the stepper motor used in this thesis. The spatial resolution of the LCTV may be a limiting factor for the filter (rather than the crystal), but the TV

could be removed for spatial resolution experiments.

## 8.2 *Switchable Adder/Subtractor*

In this thesis an electronically switchable optical adder/subtractor was successfully designed and demonstrated. The Michelson interferometer performed coherent image subtraction and incoherent image addition as a consequence of the PCM and an extra length used in one leg.

It is recommended that additional research be conducted to fully characterize the switchable adder/subtractor. Additional research is required to investigate the duty cycle of changing images, set-up time for adding and subtracting, and the spatial resolution of the system. In addition, phase and polarization modulations of input images should be evaluated and compared to the amplitude modulation used in this thesis.

It is also recommended that spatial light modulators or liquid crystal TVs (LCTVs) replace the two input transparencies to investigate the system's ability to handle grey scale images. Two grey levels (black and white) were used in this thesis, but the theoretical analysis presented in Chapter VI indicates that the adder/subtractor will properly handle grey scale images.

Finally, alternate Michelson interferometer configurations, an example is shown in Figure 19, should be evaluated and compared to the configuration used in this thesis. Alternate configurations offer reduced optical components which could increase the efficiency and performance of the adder/subtractor.

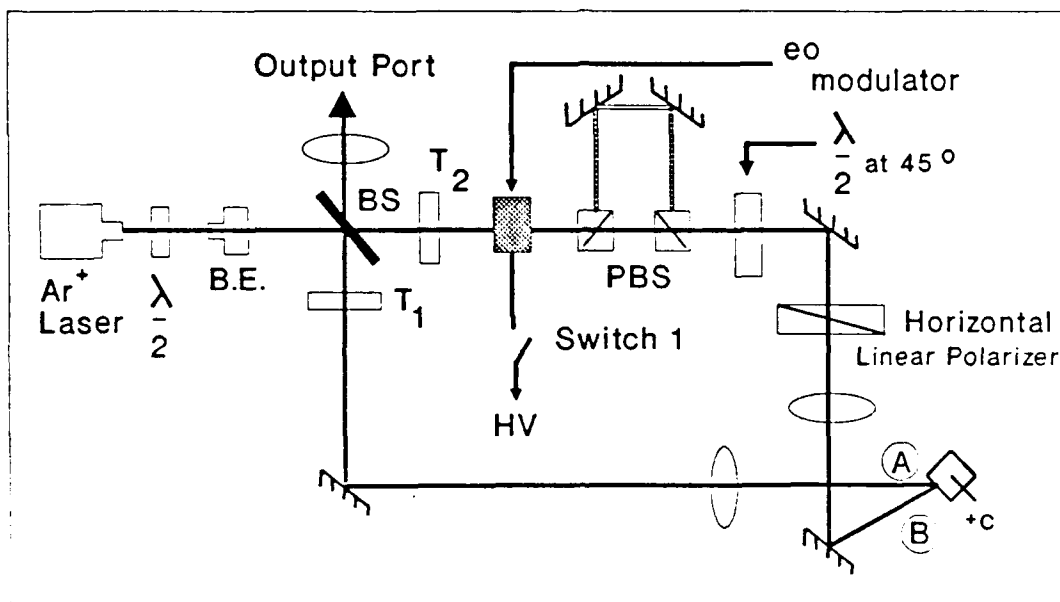


Figure 19. An alternate configuration for the switchable optical adder/subtractor.



## Appendix A. General References

The references listed below were not specifically cited in the thesis but provided the necessary background information to fully understand the concepts presented. They are included here to serve as a starting point for further research.

Bledowski, Aleksander and Wieslaw Krolikowski. "Exact Solution of Degenerate Four-Wave Mixing in Photorefractive Media," *Optics Letters*, 13: 146-148 (February 1988).

Erdmann, Andreas and Richard Kowarschik. "Theory of Degenerate Four-Wave Mixing in Anisotropic, Optically Active Photorefractive Crystals," *IEEE Journal of Quantum Electronics* 24: 155-161 (February 1988).

Fisher, Robert A. *Optical Phase Conjugation*. New York: Academic Press, 1983.

Kalinin, V. A. and L. Solymar. "Numerical Solution of Four-Wave Mixing in Passive Phase Conjugate Mirrors," *IEEE Journal of Quantum Electronics*, 24: 2070-2075 (October 1988).

Kong, Hongzhi *et al.* "Photorefractive Phase Conjugation With Orthogonally Polarized Pumping Beams," *Optics Letters*, 13: 324-326 (April 1988).

Kwong, Sze-Keung *et al.* "Real Time Image Subtraction and 'Exclusive Or' Operation Using a Self-Pumped Phase Conjugate Mirror," *Applied Physics Letters*, 48: 201-203 (January 1986).

Marciniak, Michael A. *Nonlinear Optical Principles and The Photorefractive Effect Applied to Optical Phase Conjugation*. MS thesis, AFIT/GEO/ENP/87D-3. School of Engineering, Air Force Institute of Technology (AU), Wright-Patterson AFB OH, December 1987 (AD-A188856).

McMichael, Ian and Pochi Yeh. "Phase Shifts of Photorefractive Gratings and Phase-Conjugate Waves," *Optics Letters*, 12: 48-50 (January 1987).

Petersen, Paul M. and Per Michael Johansen. "Simple Theory for Degenerate Four-Wave Mixing in Photorefractive Media," *Optics Letters* 13: 45-46 (January 1988).

Tajima, Kazuhito and Hsiung Hsu. "Theory of Mode Hopping and Phase Conjugation Characteristics in Degenerate Four-Wave Mixing," *IEEE Journal of Quantum Electronics*, 24: 1893-1907 (September 1988).

Vachss, Frederick and Lambertus Hesselink. "Synthesis of a Holographic Image Velocity Filter Using The Nonlinear Photorefractive Effect," *Applied Optics*, 27: 2887-2894 (July 1988).

White, Jeffrey O. *et al.* "Coherent Oscillation by Self-Induced gratings in the Photorefractive Crystal BaTiO<sub>3</sub>," *Applied Physics Letters*, 40: 450-452 (March 1982).

Yariv, Amnon. *Optical Electronics* (Third Edition). New York: Holt, Rinehart and Winston, 1985.

Yariv, Amnon and Pochi Yeh. *Optical Waves in Crystals*. New York: John Wiley & Sons, 1984.

Ye, Peixian *et al.* "Mutually Coherent Beam Induced Self-Pumped Phase Conjugate Reflection in BaTiO<sub>3</sub>," *Applied Physics Letters*, 55: 830-831 (August 1989).

Yeh, Pochi. "Fundamental Limit of The Speed of Photorefractive Effect And Its Impact On Device Applications And Material Research," *Applied Optics*, 26: 602-604 (February 1987).

## Appendix B. *Computer Generated Holograms*

The generation, photoreduction, and usage of the computer generated holograms are detailed in this Appendix. The FORTRAN program used to generate the holograms is discussed followed by the process of reducing the holograms onto glass slides. Finally, a few tips on using the holograms in optical systems is presented at the end of this appendix.

### B.1 *Program*

The following program is a modified version of the computer generated hologram program written by Robinson (14:37). The program was modified to allow sinusoidal holographic patterns to be generated and the ability to allow the user to specify plot filenames.

```
c *****
c
c Demonstration of Detour Phase CGH
c Written by Vicki Robinson
c Edited by Gordon Hengst
c
c *****
```

```
character*25 filename
integer      cycles
```

Parameter (D=64, pi=3.14159265, P=1, Q=0)

```
write (6,3000) "Plot filename to be created: "
3000 format (a30)
read (5,2000) filename
2000 format (a10)
```

```

write (6,3000) "Number of cycles per cm: "
read (5,4000) cycles
4000 format (i4)

Call Setplot(filename,1,0,.false.)
Call mapxy(0.,1.,0.,1.,0.,1.,0.,1.,0,1)
Do 30 m = 1, D
Do 20 n = 1, D
hmag = (sin(2*pi*cycles*m/D) + 1)/2
Call box(m,n,hmag)
20 Continue
30 Continue
Call Endplot
Stop
End
c *****
Subroutine box(m,n,hmag)
Parameter (iboxw=35,iw=17,ihmax=35,iosx=500,iosy=90)
icx = m*iboxw - (iboxw/2) + iosx
icy = n*iboxw - (iboxw/2) + iosy
ih = ihmax * hmag
ilx = icx - (iw/2)
ily = icy - (ih/2)
Do 10 i = ilx,ilx + iw
Call drv(i,ily,i,ily+ih)
10 Continue
Return
End

```

The program uses METALIB, a program library on GALAXY, to create the plot file. The file will contain the specified number of cycles in the x-direction while maintaining a constant value in the y-direction.

To compile the program on GALAXY, use the command

```
f77 filename.f -ofilename -lmetalib
```

The '-o' option allows the user to specify the name of the \*.exe file (default is aout.exe). The alternate library used by the program is specified by the '-l' option.

The program is run by typing the name specified at the '-o' option. The program will create the plot file *pltname.plt*. NOTE: The program does not check to see if a plot filename already exists; it will over write the file.

To print the plot files on GALAXY, use the command:

```
mit pltname —lpr -Pimagen
```

The files are very large and usually take about 15 minutes to plot. At the time of this thesis, the printer IMAGEN was located in the second floor printer room, Bldg 642. The output from the printer will be similar to Figure 20 which shows 4 cycles.

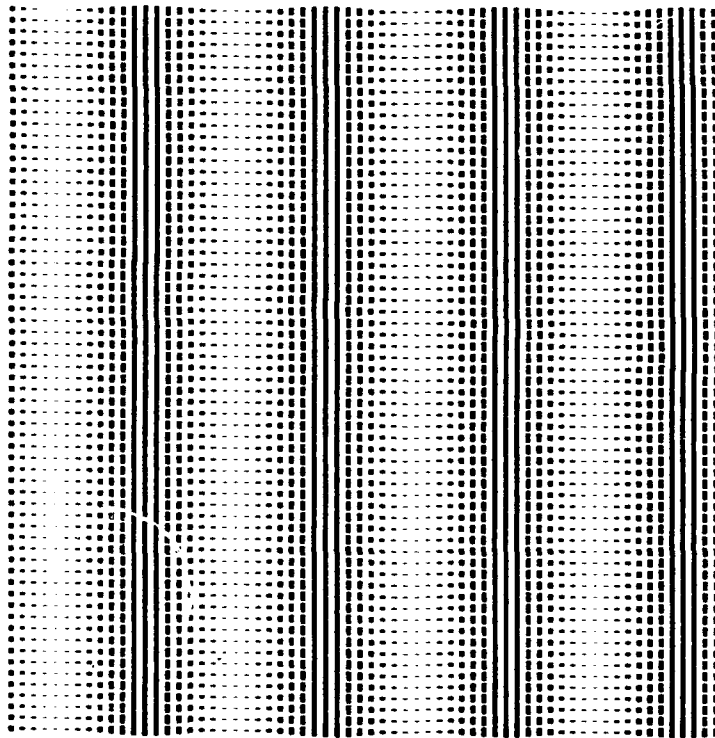


Figure 20. A sinusoidal computer generated hologram showing 4 cycles

### *B.2 Photoreduction of Holograms*

Once the hologram is printed, it will need to be reduced onto glass for use in the optical system. The equipment used to photoreduce the computer generated holograms is located in the Cooperative Electronics Materials Processes Laboratory.

room 1065, in building 125. Prior to photoreducing, the printed hologram is transferred to an overhead transparency with either a XEROX copier or a Thermofax transfer machine. The Thermofax is recommended since the contrast is better than the copier. The transparency will serve as the negative for the photoreduction process.

The Dekacon photoreduction system shown in Figure 21 can reduce the original hologram from 10X to 60X depending on the settings chosen from the camera manual. For this thesis, two holograms were made using the 60X setting and a 1 min exposure time. To further reduce the hologram, the original hologram was shrunk by 50% on a copier before the Thermofax transfer was made. Using this technique allows a reduction of close to 120X possible. After exposure, the film plate was developed using 2 min in the developer and 1 min each for the stop and fixer. The final product resolutions of the glass slides is shown in Table 4.

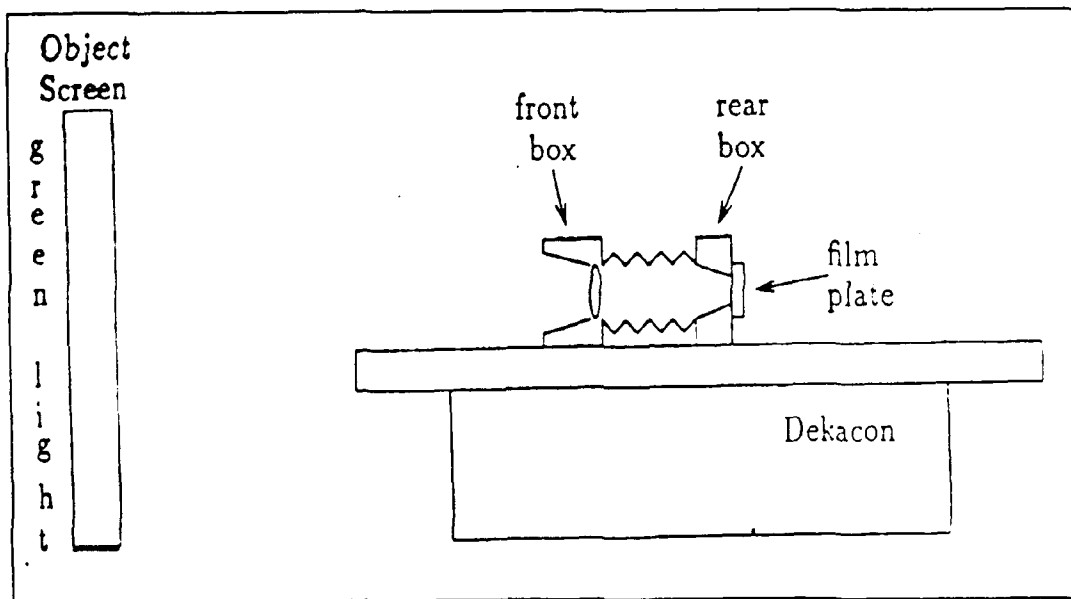


Figure 21. Dekacon photoreduction system. (14:43)

<i># of cycles</i>	<i>Final CGH size</i>	<i>Resolution</i>
4	0.161 cm	24.8 cyc/cm
8	0.155 cm	51.6 cyc/cm

Table 4. Resolutions of computer generated holograms obtained using a 50% reduced transparency and 60X photoreduction

### *B.3 Tips On Hologram Usage*

1. Since the original hologram consists of discrete blocks, the fourier transform is periodic. As the photoreduction of the original hologram is increased, the period between transforms also increases. These extra, periodic transforms can be easily filtered out by placing an iris in the fourier plane to allow only the fundamental transform to pass through.
2. The glass slides are sensitive to high power densities. The photo resist coatings on the holograms begins to discolor when approximately 3 W is focused onto the hologram. It is recommended that the holograms be placed in an expanded beam where the power density is low.
3. The laser beam should be expanded well beyond the aperture limits of the hologram. This will alleviate the underlying gaussian profile that occurs if the beam is not expanded enough as shown in Figure 22.

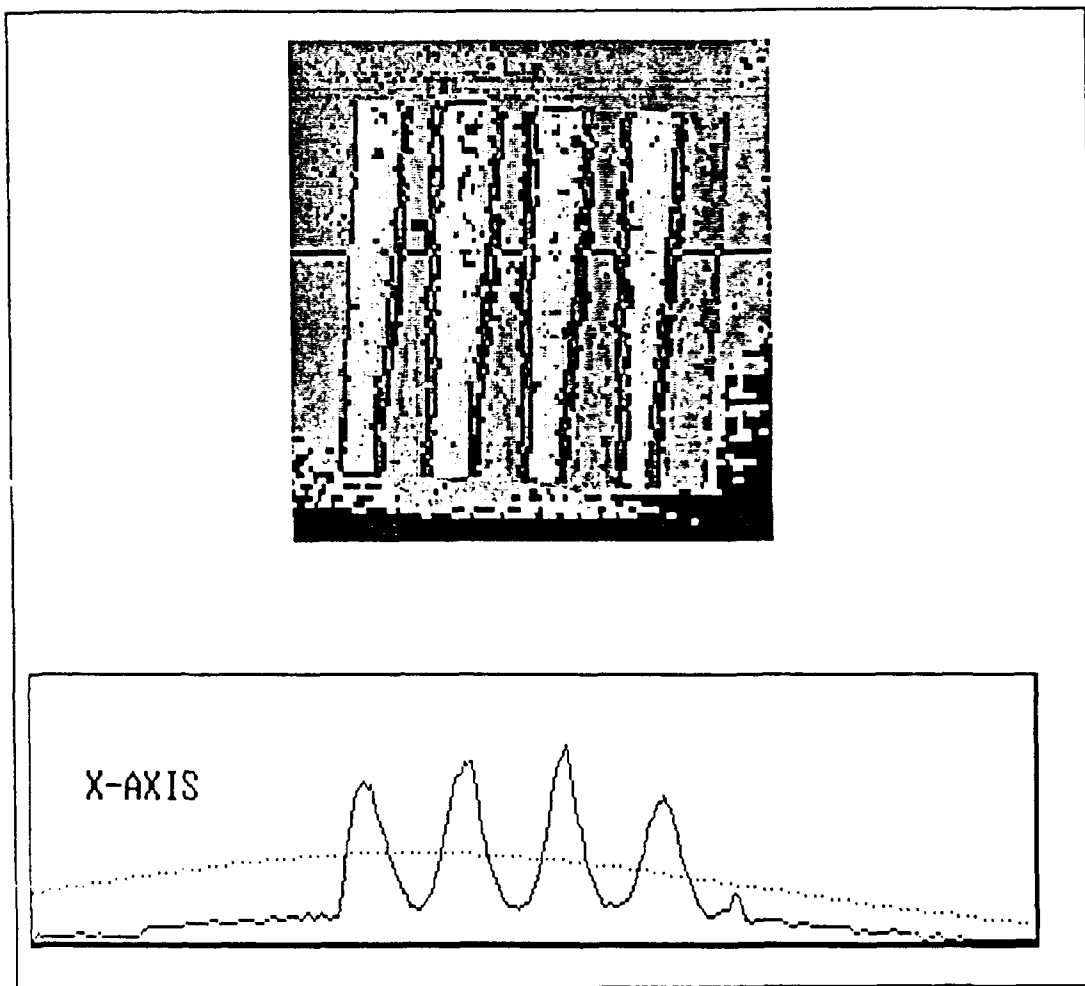


Figure 22. Intensity profile of a 4 cycle computer generated hologram showing the sinusoidal profile. The gaussian profile of the laser beam incident on the hologram is shown by the dotted line.



## Appendix C. *Experimental Procedure for Determining Onset Time*

The experimental process discussed below was used in the thesis to determine  $\tau_{filter}$  for each crystal sample. Figure 23 shows the experimental set-up. An iris was inserted behind the crystal to shield the output signal from the beam fanning. Each crystal was oriented such that the signal beam intersected the crystal axis at  $45^\circ$  and the fanning would spread away from the detector (note: if the crystal fans toward the detector, flip it end-for-end, i.e., point the +c in the opposite direction). Various chart recorder speeds were selected depending on the response of the crystal and the input power.

### *Experimental Procedure*

1. With the signal beam on, erase any gratings in the crystal by orienting it at any angle other than  $45^\circ$ .
2. Block the signal beam and orient the crystal to  $45^\circ$ .
3. Set the incident intensity level.
4. Start the chart recorder and unblock the signal beam.
5. When steady state has been reached, measure the intensity just prior to the crystal surface.
6. Repeat steps 1-5 for each intensity level. The chart recorder traces will be similar to the one shown in Figure 24.
7.  $\tau_{filter}$  is determined by the 50% point on each trace as shown in Figure 24.

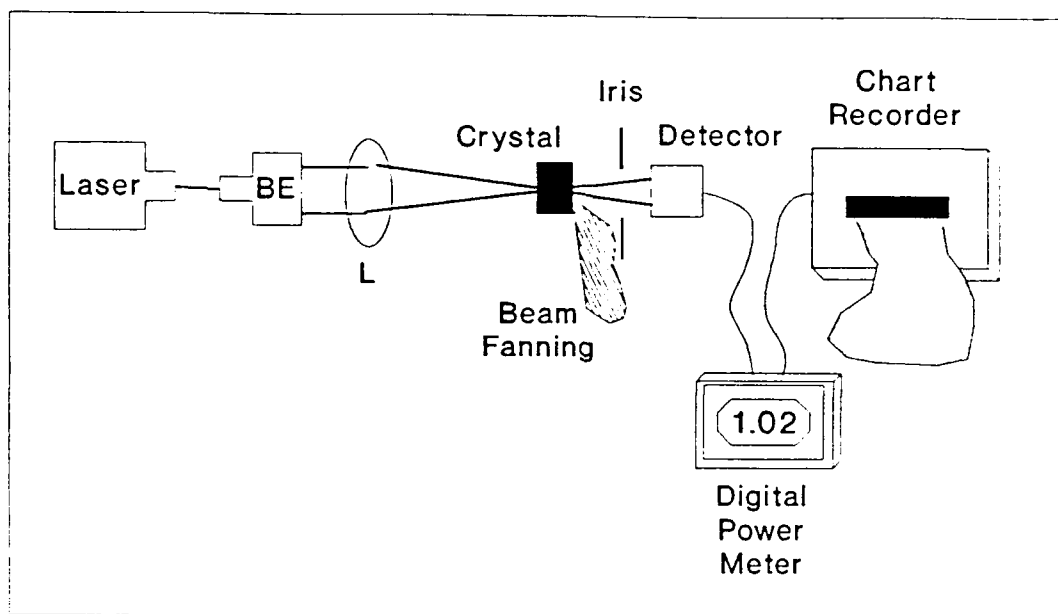


Figure 23. Experimental set-up to determine the onset time for each crystal.

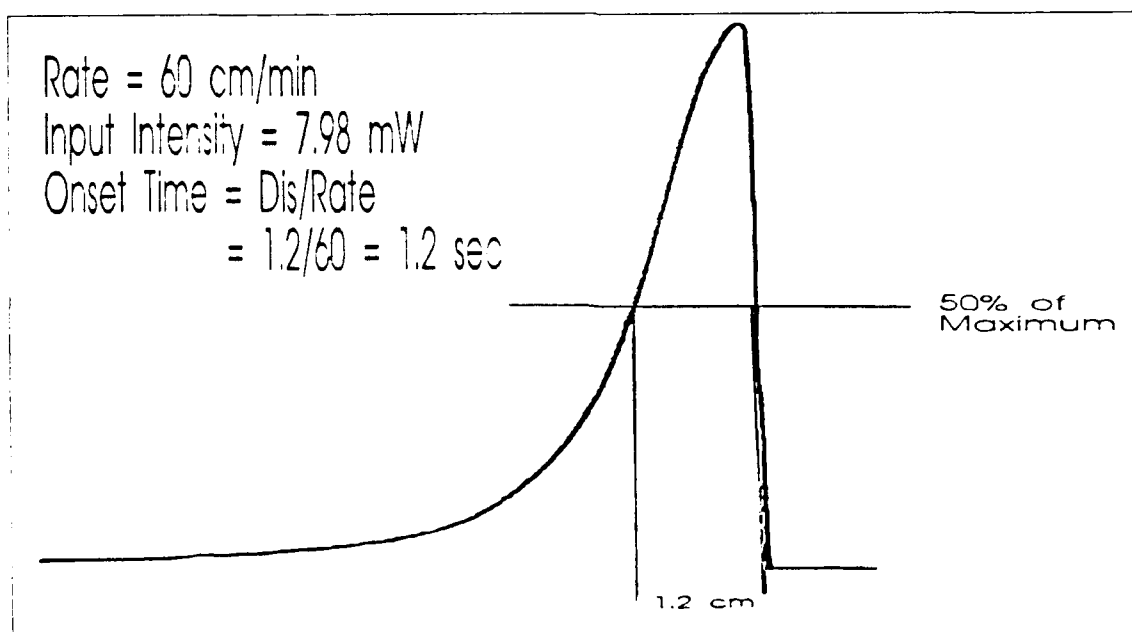


Figure 24. Sample filter trace to determine the crystal's onset time,  $\tau_{filter}$ .

## Bibliography

1. Anderson, Dana Z. *et al.* "Optical Tracking Novelty Filter," *Optics Letters*, 12: 123-125 (February 1987).
2. Anderson, Dana Z. and Jack Feinberg. "Optical Novelty Filters," *IEEE Journal of Quantum Electronics*, 25: 635-647 (March 1989).
3. Bledowski, Aleksander and Wieslaw Krolikowski. "Anisotropic Four-Wave Mixing In Cubic Photorefractive Crystals," *IEEE Journal of Quantum Electronics*, 4: 652-658 (April 1988).
4. Chiou, Arthur E. and Pochi Yeh. "Parallel Image Subtraction Using a Phase-Conjugate Michelson Interferometer," *Optics Letters*, 11: 306-308 (May 1986).
5. Chiou, Arthur E. *et al.* "Nonlinear Optical Image Subtraction for Potential Industrial Applications," *Optical Engineering*, 27: 385-392 (May 1988).
6. Cronin-Golomb, Mark *et al.* "Passive (Self-Pumped) Phase Conjugate Mirror: Theoretical and Experimental Investigation," *Applied Physics Letters* 41: 689-691 (October 1982).
7. Cronin-Golomb, Mark *et al.* "Photorefractive Time Differentiation of Coherent Optical Images," *Optics Letters*, 12: 1029-1031 (December 1987).
8. Ewbank, M. D. *et al.* "Time Reversal By An Interferometer With Coupled Phase-Conjugate Reflectors," *Optics Letters*, 10: 282-284 (June 1985).
9. Feinberg, Jack. "Self-Pumped, Continuous-Wave Phase Conjugator Using Internal Reflection," *Optics Letters*, 7: 486-488 (October 1982).
10. Feinberg, Jack. "Interferometer With a Self- Pumped Phase-Conjugating Mirror," *Optics Letters*, 8: 569-571 (November 1983).
11. Ford, Joseph E. *et al.* "Time-Integrating Interferometry Using Photorefractive Fanout," *Optics Letters*, 13: 856-858 (October 1988).
12. Knittl, Zdenek. *Optics of Thin Films*. New York: John Wiley & Sons, Ltd, 1976.
13. Pepper, David M. *et al.* "The Photorefractive Effect," *Scientific American*, 62-74 (October 1990).
14. Robinson, Vicky Lynn. *Hybrid Calculation of Invariant Moments*. MS thesis. AFIT/GEO/ENG/88D-3. School of Engineering, Air Force Institute of Technology (AU), Wright-Patterson AFB OH, December 1988 (AD-A202594).
15. Tomita, Yasuo, *et al.* "Real-Time Image Subtraction With the Use of Wave Polarization and Phase Conjugation," *Applied Physics Letters*, 52: 425-427 (February 1988).

16. Wink, Karen A. *Laser Beam Coupling Via Optical Phase Conjugation In BaTiO<sub>3</sub>*. MS thesis, AFIT/GEP/ENP/88D-7. School of Engineering, Air Force Institute of Technology (AU), Wright-Patterson AFB OH, December 1988 (AD-A202874).

## *Vita*

Captain Gordon T. Hengst [REDACTED]

[REDACTED] He graduated high school and attended The Pennsylvania State University in College Park, Pennsylvania, from which he received the degree of Bachelor of Science in Electrical Engineering in May 1985. Upon graduation, he received a commission in the USAF through the ROTC program. Captain Hengst was assigned as an electrical engineer at the Avionics Laboratory, Wright Research and Development Center, Aeronautical Systems Division, until entering the School of Engineering, Air Force Institute of Technology, in May 1989. Captain Hengst will be assigned to the Air Force Weapons Laboratory, Kirtland AFB, NM, as his follow-on assignment to AFIT.

[REDACTED]

REPORT DOCUMENTATION PAGE			Form Approved OMB No. 0704-0188	
<small>Public reporting burden for this collection of information is estimated to average 1 hour per response, including the time for reviewing instructions, searching existing data sources, gathering and maintaining the data needed, and completing and reviewing the collection of information. Send comments regarding this burden estimate or any other aspect of this collection of information, including suggestions for reducing this burden, to Washington Headquarters Services, Directorate for Information Operations and Reports, 1215 Jefferson Davis Highway, Suite 1204, Arlington, VA 22202-4302, and to the Office of Management and Budget, Paperwork Reduction Project (0704-0188), Washington, DC 20503</small>				
1. AGENCY USE ONLY (Leave blank)	2. REPORT DATE December 1990	3. REPORT TYPE AND DATES COVERED Master's Thesis		
4. TITLE AND SUBTITLE NONLINEAR INTERFEROMETRY: OPTICAL IMAGE ADDITION/SUBTRACTION AND NOVELTY FILTERS		5. FUNDING NUMBERS		
6. AUTHOR(S) Gordon T. Hengst, Captain, USAF				
7. PERFORMING ORGANIZATION NAME(S) AND ADDRESS(ES) Air Force Institute of Technology, WPAFB OH 45433-6583		8. PERFORMING ORGANIZATION REPORT NUMBER AFIT/GEO/ENP/90D-2		
9. SPONSORING/MONITORING AGENCY NAME(S) AND ADDRESS(ES)		10. SPONSORING/MONITORING AGENCY REPORT NUMBER		
11. SUPPLEMENTARY NOTES				
12a. DISTRIBUTION/AVAILABILITY STATEMENT Approved for public release; distribution unlimited  Doz.		12b. DISTRIBUTION CODE		
13. ABSTRACT (Maximum 200 words) This thesis investigated the performance characteristics of a beam fanning novelty filter and designed a switchable optical image adder/subtractor. The filter spatial resolution, contrast ratio, onset time, and velocity response were measured for both z-cut and 45°-cut BaTiO <sub>3</sub> crystals in the beam fanning configuration. Experimental results show that the special 45°-cut crystal produces the best overall beam fanning novelty filter. In addition, switchable optical image subtraction and addition were demonstrated for the first time using a modified Michelson interferometer configured with a phase-conjugating mirror and an adjustable length leg. The system demonstrated addition and subtraction with one-dimensional and two-dimensional images. The adder/subtractor can be switched from coherent subtraction to incoherent addition by biasing a set of e-o crystals which switches the beam in one of the legs of the interferometer into an extra length. The extra length is greater than the coherence length of the laser so that incoherent addition results. The thesis concludes with a brief discussion of industrial and military system applications of the novelty filter and adder/subtractor. <i>Keywords:</i>				
14. SUBJECT TERMS Novelty Filter, Image Addition, Image Subtraction, Phase-Conjugation, Velocity Filter, Beam Fanning, (762) / C			15. NUMBER OF PAGES 60	
			16. PRICE CODE	
17. SECURITY CLASSIFICATION OF REPORT Unclassified	18. SECURITY CLASSIFICATION OF THIS PAGE Unclassified	19. SECURITY CLASSIFICATION OF ABSTRACT Unclassified	20. LIMITATION OF ABSTRACT UL	